water

MDPI

Article

Decoupling Capacitance from Desalination Performance in Polyaniline-Modified Carbon Electrodes with Different Porosity for Capacitive Deionization

Alexander Yu. Zakharov [1,2,†], Sagydat Duisenbekov [3,†], Georgiy V. Alexan [1,2,4], Guldana Zhigerbayeva [5], Zhanibek Ayaganov [1,2], Salimgerey Adilov [6], Vladimir V. Pavlenko [1,2,4,7,*] and Nurxat Nuraje [3,5,*]

1 The Institute of Combustion Problems, Almaty 050012, Kazakhstan
2 Nazarbayev University Research Administration, Astana 010000, Kazakhstan
3 Department of Chemical Engineering, School of Engineering & Digital Science, Nazarbayev University, Astana 010000, Kazakhstan
4 Carbonix Group LLP, Almaty 050012, Kazakhstan
5 Laboratory of Renewable and Hybrid Energy Systems, Institute of New Materials and Energy Technologies, Astana 010000, Kazakhstan
6 Department of Chemistry, School of Sciences and Humanities, Nazarbayev University, Astana 010000, Kazakhstan
7 UNESCO Chair for Sustainable Development, al-Farabi Kazakh National University, Almaty 050040, Kazakhstan
* Correspondence: vladimir.pavlenko@kaznu.edu.kz (V.V.P.); nurxat.nuraje@nu.edu.kz (N.N.)
† These authors contributed equally to this work.

Abstract

Carbon electrodes for capacitive deionization (CDI) are usually ranked by capacitance measured under conditions different from those of desalination. Six electrodes—a microporous activated carbon from waste coffee grounds, a micro-mesoporous templated carbon from magnesium citrate, their 1:1 mixture, and each with 5 wt% polyaniline (PANI)—were characterized electrochemically in 1 M H_2SO_4 and in the NaCl feed at the CDI cell voltage, and tested in batch-mode CDI at +1.6 V. For the three pristine electrodes, capacitance ranked the initial salt adsorption capacity (SAC) correctly in both electrolytes and by every technique, and their 1:1 mixture showed no synergy under the conditions tested. PANI raised the capacitance by 16–18% in acid, but in the feed its contribution varied between the carbons, was partly irreversible and did not follow the SAC, which fell for the coffee-waste carbon and rose for the templated one. No electrochemical measurement anticipated durability: all electrodes retained 95–100% of their capacitance over 10,000 cycles in acid, whereas the pristine ones lost most of their SAC within 100 CDI cycles, and PANI raised the mean SAC retention of the templated carbon from 12% to 76%. Capacitance is thus a useful first screen for purely capacitive carbons, but not for electrodes with a pseudocapacitive component or for predicting service life.

Keywords: activated carbons; capacitive deionization (CDI); modified electrodes; cycling stability; polyaniline; pseudocapacitance; pore architecture

Check for updates

Academic Editor: Jesus Gonzalez-Lopez

Received: 25 September 2026
Revised: 26 October 2026
Accepted: 28 October 2026
Published: 01 November 2026

Copyright: © 2026 by the authors. Licensee MDPI, Basel, Switzerland. This article is an open access article distributed under the terms and conditions of the Creative Commons Attribution (CC BY) license.

1. Introduction

The desalination performance of a capacitive deionization electrode is conventionally optimized through its porous texture and its capacitance, by maximizing the volume of pores narrow enough to store charge efficiently and, increasingly, by introducing pseudocapacitive components that add faradaic storage to the electrical double layer [1–3]. As with

carbon adsorbents in water treatment generally, the practical value of such electrodes depends not only on their initial capacity but also on how much of it is retained over repeated regeneration cycles [4]. Yet the same electrodes lose the greater part of that capacity within tens of cycles when operated at the cell voltages that make the process practically attractive, as the positively polarized electrode is progressively oxidized [4–6]. For electrodes operated at such voltages, capacity and durability are therefore not two independent figures of merit to be improved in turn, and they can become competing criteria: the quantity that determines how much salt an electrode removes over its service life is not the capacity it starts with, but the fraction of that capacity it still possesses after a realistic number of cycles. This distinction is rarely made explicit, and the two properties are commonly assessed under conditions that have little in common. Salt adsorption capacities are reported for the first cycles, electrochemical stability is measured by galvanostatic cycling within a voltage window in which water is thermodynamically stable, and desalination stability is measured in a neutral chloride solution at a cell voltage that exceeds that window [7,8]. The two are then treated as interchangeable indicators of the same material property.

Strategies developed to address the durability problem reflect this separation. Restricting the cell voltage, redistributing the potential between the two electrodes through asymmetric operation or asymmetric electrode masses, inverting the adsorption–desorption sequence, and interposing an ion-exchange membrane or a polymer barrier between the carbon and the electrolyte have all been shown to extend electrode life substantially [5–7,9,10]. What these approaches have in common is that they act at the level of the cell and its operating protocol rather than at the level of the electrode material: they reduce the oxidative stress the carbon experiences instead of changing how the carbon responds to it. The complementary question—whether the material itself can be formulated so that the capacity it delivers is also the capacity it retains—is addressed far less often, and is not answered by the capacity measurements through which electrode materials are usually compared.

Two of the most common material-level optimization strategies are worth examining in this light, because both are justified by mechanisms whose relevance to the operating conditions of a CDI cell is not self-evident. The first is the construction of hierarchical micro-mesoporous architectures, in which mesopores are expected to act as transport channels feeding the micropores that store the charge [2,3,11]. The rate advantage this confers is real in electrochemical measurements, but a CDI half-cycle lasts minutes, and whether ion transport is limiting on that timescale is rarely tested; indeed, a systematic comparison of porous carbons found salt adsorption to correlate positively with the volume of pores below one nanometer and negatively with total pore volume and BET area, contrary to the expectation that mesopores are required [1]. The second is the incorporation of conducting polymers such as polyaniline, which adds pseudocapacitance and has been reported to improve capacitance, wettability and cycle life of carbon CDI electrodes [12,13]. Here the difficulty is that the redox chemistry responsible for the added capacity is proton-coupled, so that the gain measured in an acidic electrolyte need not survive the transfer to the neutral feed water in which desalination is actually performed. In both cases the mechanism invoked to justify the modification operates under conditions other than those in which the electrode is used.

In this work, two carbons with contrasting pore textures were selected for comparison: a microporous activated carbon obtained by KOH activation of waste coffee grounds and a micro-mesoporous carbon produced by self-templating from magnesium citrate; a 1:1 physical mixture of the two carbons was also examined. Each of the three carbon architectures was studied with and without 5 wt% polyaniline nanofibers incorporated into the electrode formulation, yielding six compositions that differ in pore architecture and pseudocapacitive content while sharing the same binder, electrode geometry, and preparation procedure. To

test whether measurements in the feed itself are a better guide to desalination than those in acid, the electrodes were characterized both in sulfuric acid and in the NaCl feed solution at the cell voltage used for CDI. The comparison was designed to test two assumptions that are common in the design of CDI electrodes: that mesopores added to a microporous carbon improve salt removal by easing ion transport, and that a pseudocapacitive polymer raises the salt adsorption capacity and durability of an electrode in proportion to the capacitance it adds. Unlike the previous studies of PANI-modified CDI electrodes cited above, which report the combined effect of the polymer on capacitance and desalination, the polymer loading here was kept low (5 wt%) so that the pore texture remained essentially unchanged (Table 1); this allows the effect of PANI on capacitance, initial salt adsorption and durability to be examined separately from that of the pore architecture. The results show that capacitance, whether measured in acid or in the feed itself, ranks the initial desalination performance of the purely capacitive carbons but not of the electrodes containing a pseudocapacitive component, and predicts the durability of none of them, that the 1:1 mixed-carbon electrode provides no advantage on the timescale of the CDI cycle used here, and that the effect of PANI on desalination cannot be predicted from its effect on capacitance alone. These findings provide a basis for the rational design of advanced CDI electrodes that combine sustainable carbon precursors with conductive-polymer functionalization to improve desalination performance and electrochemical stability.

Table 1. Porous texture data of the carbon materials.

Material	S_{BET}, $m^2 g^{-1}$	S_{DFT}, $m^2 g^{-1}$	$V_{total\ DFT}$, $cm^3 g^{-1}$	$V_{micro\ DFT}$, $cm^3 g^{-1}$	$V_{meso\ DFT}$, $cm^3 g^{-1}$	% of Micropores	L_{micro}, nm	L_{meso}, nm
AC-CW carbon	2941	2160	1.670	0.756	0.914	45.3	0.96	2.6
TC-MC carbon	1695	1355	2.101	0.307	1.794	14.6	0.53/1.08	3.8 [a]
PANI	35.9	-	0.166	0.007	0.158	4.5	1.2	-
AC-CW electrode	2305	1721	1.353	0.603	0.749	44.6	0.96	2.5
TC-MC electrode	1397	1140	1.948	0.242	1.706	12.4	0.53/1.09	4.6 [a]
AC-CW -P electrode	2242	1648	1.308	0.589	0.719	45.0	0.96	2.6
TC-MC-P electrode	1464	1113	1.738	0.254	1.484	14.6	0.53/1.09	3.6 [a]

Note: [a] The TC-MC mesoporous mode varies between 3.6 and 4.6 nm across replicates due to a broad polydisperse distribution without a saturation plateau; the micropore modes are stable.

2. Materials and Methods

2.1. Preparation of Carbon Electrodes

Potassium hydroxide (KOH) was purchased from Laborpharma (Almaty, Kazakhstan); magnesium citrate, sodium chloride and potassium bromide from Shanghai Macklin Biochemical Co., Ltd. (Shanghai, China); hydrochloric acid and sulfuric acid (H_2SO_4) from Labkhimprom (Almaty, Kazakhstan); ammonium persulfate, pentanol, cyclohexane, aniline and acetone from Sigma-Aldrich (St. Louis, MO, USA); and isopropyl alcohol from Carl Roth GmbH + Co. KG (Karlsruhe, Germany). All reagents were used as received.

Activated micro-mesoporous carbon from coffee wastes (CW) was manufactured following a previously reported procedure [14]. Briefly, the coffee wastes after espresso preparation were washed, dried, and carbonized at 450 ± 10 °C for 90 min under N_2 atmosphere. Chemical activation was then performed by heating the carbonized material with KOH at 800 ± 10 °C for 1 h under N_2 atmosphere, using a carbon-to-activator weight ratio of 1:4. The activated product was washed to neutral pH and dried in a vacuum at 90 °C. The activated carbon obtained by the above method will hereafter be referred to as AC-CW carbon.

Templated mesoporous carbon from magnesium citrate was manufactured as described elsewhere [11,15]. The salt was carbonized at 800 °C for 120 min under N_2 atmo-

sphere. The carbonizate was treated with a 3 M HCl solution at room temperature for 24 h. The resulting templated carbon was washed with distilled water to neutral pH and dried in a vacuum at 90 °C. The templated carbon obtained by the above method will hereafter be referred to as TC-MC carbon.

The polyaniline nanofibers were synthesized using a bicontinuous microemulsion polymerization method [16]. Initially, ammonium persulfate (APS) was dissolved in deionized water and subsequently mixed with a pentanol surfactant solution at an APS: pentanol mass ratio of 2:3. Separately, a cyclohexane/monomer solution was prepared at a weight ratio of 6:1 and then combined with the APS-containing mixture. Polymerization was initiated after the formation of the bicontinuous microemulsion phase to ensure the development of a homogeneous conducting polymer structure. The reaction mixture was maintained at room temperature for 24 h, during which green PANI particles were formed. The obtained product was collected and washed several times with acetone to remove residual impurities and unreacted monomers. The synthesized PANI nanofibers were characterized using Fourier transform infrared spectroscopy (FTIR) using a Bruker Alpha II spectrometer (Bruker Optik GmbH, Ettlingen, Germany) equipped with a Platinum single-reflection diamond ATR module, over the range 400–4000 cm^{-1} with a resolution of 4 cm^{-1} and 24 co-added scans.

Free-standing electrodes for electrochemical and CDI measurements were prepared following a standard procedure described elsewhere [17]. The electrode composition included 85 wt% carbon material, 10 wt% carbon black (Timcal C45; Imerys Graphite & Carbon, Bodio, Switzerland), and 5 wt% polytetrafluoroethylene (PTFE, 60% aqueous dispersion, Sigma-Aldrich, St. Louis, MO, USA). The mixing process was conducted using a magnetic stirrer at a temperature of 70 °C, with the addition of isopropyl alcohol to achieve a fluid consistency. Subsequently, the mixture was subjected to controlled evaporation, causing it to solidify into a dough-like mass. The resulting dough was rolled using a Doctor Blade to form electrode sheets with a thickness of approximately 100 µm. Circular electrodes with areas of 0.785 cm^2 (for electrochemical tests; d = 10 mm) and 19.63 cm^2 (for CDI experiments; d = 50 mm) were cut from these sheets using a template and subsequently dried under vacuum at 120 °C overnight. The electrodes will hereafter be referred to as simple AC-CW and TC-MC, respectively. Mixed-carbon electrodes were prepared by the same procedure, the carbon fraction consisting of AC-CW and TC-MC in a 1:1 weight ratio. These electrodes are hereafter referred to as "AC-CW + TC-MC".

Modified electrodes were prepared by the same procedure, with an electrode composition of 80 wt% carbon material, 10 wt% carbon black (Timcal C45), 5 wt% polytetrafluoroethylene (PTFE, 60% aqueous dispersion, Sigma-Aldrich) and 5 wt% PANI. The modified electrodes are hereafter referred to as AC-CW-P, TC-MC-P and (AC-CW + TC-MC)-P. The PANI loading was kept low to leave the pore texture unaltered (Section 1); higher loadings would progressively occlude the microporosity [18,19].

The typical mass loading for CDI electrodes (total mass of the two electrodes) was 141.40 ± 2.64 mg for AC-CW, 157.40 ± 7.63 mg for TC-MC, 142.70 ± 12.41 mg for AC-CW+TC-MC, 102.20 ± 4.06 mg for AC-CW-P, 146.60 ± 4.82 mg for TC-MC-P and 121.80 ± 12.41 mg for (AC-CW + TC-MC)-P. For electrochemical measurements the typical mass loading (total mass of the two electrodes) was 5.63 ± 0.51 mg for AC-CW, 4.67 ± 0.16 mg for TC-MC, 5.13 ± 0.11 mg for AC-CW + TC-MC, 6.07 ± 0.18 mg for AC-CW-P, 4.30 ± 0.17 mg for TC-MC-P and 4.67 ± 0.22 mg for (AC-CW + TC-MC)-P, respectively. This corresponds to areal loadings of 3.6, 4.0, 3.6, 2.6, 3.7 and 3.1 mg cm^{-2} per electrode for the CDI electrodes and 3.6, 3.0, 3.3, 3.9, 2.7 and 3.0 mg cm^{-2} per electrode for the electrodes used in electrochemical measurements, in the same order, at an electrode thickness of approximately 100 µm.

2.2. Characterization of Carbon Electrodes

The specific surface area and pore structure were analyzed by low-temperature nitrogen adsorption–desorption at 77K using a BSD-660M Porosity Analyzer (BSD Instrument, Beijing, China). Powders were degassed at 200 °C for 300 min; PANI-containing electrodes were degassed at 120 °C for 600 min, since polyaniline in the emeraldine salt form begins to lose its dopant above ~150 °C. Mass loss on degassing was 11–14% for the powders and 1.6–3.6% for the electrodes. The saturation pressure was measured at every point and averaged 92.6 kPa, corresponding to a bath temperature of approximately 76.6 K at the altitude of the laboratory. Specific surface areas were calculated by the multipoint BET method over relative pressure ranges selected automatically according to ISO 9277. Pore size distributions were obtained from the adsorption branch using the HS-2D-NLDFT kernel for nitrogen at 77 K in slit-shaped carbon pores with heterogeneous surfaces (Micromeritics Instrument Corp., Norcross, GA, USA) [20], covering pore widths from 0.4 to 50 nm. The kernel was converted from a surface-area to a pore-volume basis (factor 2/W) using a liquid-nitrogen molar volume of 34.68 cm^3 mol^{-1}. The inversion was performed with an in-house Python script (Python 3.12; Python Software Foundation, Wilmington, DE, USA) using NumPy 2.5 and SciPy 1.18. The distribution dV/dlnW was represented as a non-negative combination of 36 cubic B-splines on a uniform ln W grid, and the inverse problem was solved by non-negative least squares with Tikhonov regularization. The regularization used a second-derivative penalty, and the regularization parameter was selected by the L-curve criterion. Residuals were weighted by $1/(Q + 0.02 \cdot Q_{max})$ to retain the contribution of the low-pressure points. The script reproduced the pore volume and surface area given by the instrument software to within 1% for six reference samples.

The surface morphology of the samples was examined using a CIQTEK SEM5000Pro scanning electron microscope (CIQTEK Co., Ltd., Hefei, China) equipped with Oxford Instruments X-Plore 30 (SDD) energy-dispersive X-ray microanalysis system (Oxford Instruments NanoAnalysis, High Wycombe, UK). Water contact angles were measured with a Krüss DSA25E drop shape analyzer (KRÜSS GmbH, Hamburg, Germany) using 5 µL droplets of distilled water. The droplet profile was recorded for 90 s at 30 fps; the first 10 s were discarded, and the reported angle is the mean of the left and right angles averaged over the record. FTIR spectra of the electrodes before and after 100 CDI cycles were recorded on the same Bruker Alpha II spectrometer (Section 2.1); after cycling, the positive and negative electrodes of each cell were analyzed separately. A fragment of approximately 1/6 of each electrode was ground with KBr (1:100 by mass) to dilute the strongly absorbing carbon and obtain a representative sample, and spectra were acquired with 24 co-added scans at a resolution of 4 cm^{-1}. A confocal Raman spectrometer (LabRAM, HORIBA France SAS, Palaiseau, France) with a 532 nm Nd:YAG solid-state laser for carbon samples and a 785 nm laser for polyaniline, along with a thermoelectrically cooled CCD detector, was used to measure Raman emission intensity in the range 100–3000 cm^{-1} for carbon samples and 100–1800 cm^{-1} for polyaniline sample. The instrument setup: the objective—×50, grating—600 g mm^{-1}, acquisition time—60 s, hole—300 µm, and accumulation—5 scans are collected from each sample before averaging. The D and G band region of the carbon spectra was fitted over 800–2000 cm^{-1} after subtraction of a linear baseline in OriginPro 2021 (OriginLab Corporation, Northampton, MA, USA). The envelope was decomposed into five components adapted from the model of Sadezky et al. [21]: the D1, G and D2 bands were described by Lorentzian functions and the D3 and D4 bands by Gaussian functions. During the fit the band positions were constrained to the intervals 1180–1220 (D4), 1330–1360 (D1), 1480–1520 (D3), 1570–1600 (G) and 1600–1620 cm^{-1} (D2), while amplitudes and widths were constrained only to be positive. The area of each component was

calculated analytically from its fitted amplitude and width, and the degree of graphitization was obtained from Equation (1):

$$G, \% = \frac{A(G)}{\sum_{800}^{2000} A} \times 100\% \quad (1)$$

Cyclic voltammetry (CV) at various scan rates, galvanostatic charge–discharge (GCD) tests at various current densities and electrochemical impedance spectroscopy measurements were carried out in Swagelok type 2E cells with stainless steel current collectors and 1M H_2SO_4 electrolyte using a Corrtest CS2350 potentiostat-galvanostat (Wuhan Corrtest Instruments Corp., Ltd., Wuhan, China). The equations used to calculate the electrochemical parameters are provided in the Supplementary Materials. Two-electrode cells were also characterized using electrochemical impedance spectroscopy (EIS) in the frequency range from 500 kHz to 10 mHz with an amplitude of 10 mV at 0 V. Long-term cycling stability was evaluated by GCD measurements at 2 A g^{-1} over 10,000 cycles in the same two-electrode configuration using Neware BTS4000-5V50mA battery testing system (Neware Technology Co., Ltd., Shenzhen, China), with the capacitance retention and the coulombic efficiency recorded for every cycle.

To assess whether the electrochemical behavior measured in acid is relevant to the desalination conditions, all six formulations were also characterized in the CDI feed solution, 1 g L^{-1} NaCl (17.1 mmol L^{-1}), in two-electrode cells with glassy carbon current collectors, using electrodes 8 mm in diameter (0.503 cm^2) cut from the same sheets. The total mass of the two electrodes was 3.5, 3.3, 2.9, 4.6, 2.6 and 3.3 mg for AC-CW, TC-MC, AC-CW + TC-MC, AC-CW-P, TC-MC-P and (AC-CW + TC-MC)-P, respectively, i.e., 2.6–4.6 mg cm^{-2} per electrode. The cell voltage window was extended to 0–1.6 V, the sorption voltage of the CDI experiments. Each cell was measured without disassembly in the sequence CV at 2–50 mV s^{-1}, GCD at 0.2–5 A g^{-1} and EIS at 0 V (500 kHz-10 mHz, amplitude 10 mV); one cell was measured per formulation. Because of the low conductivity of the dilute electrolyte, the ohmic drop at 2 A g^{-1} and above exceeded half of the voltage window, and GCD data are therefore reported for 0.2–1 A g^{-1} only. The coulombic efficiency was calculated as the ratio of the discharge to the charge time in GCD and of the cathodic to the anodic charge in CV.

2.3. CDI Measurements

The custom-designed CDI cell consisted of two acrylic plates with circular titanium current collectors in contact with carbon electrodes (S = 19.63 cm^2). The electrodes were separated by a 0.6 mm nylon mesh spacer. The assembly was secured using bolts and nuts, with silicone gaskets ensuring leak-tight operation (Figure S1). The cell was assembled in a symmetric setup: both electrodes were made of the same material. The experimental setup included a potentiostat-galvanostat, a peristaltic pump with controlled flow rate (17 mL·min^{-1}), a liquid reservoir, and Bante 900 multiparameter meter with CON-1 electrode (Bante Instruments Co., Ltd., Shanghai, China). The sorption step was performed at an applied voltage of +1.6 V, while desorption was conducted at 0 V; each step was maintained for 10 min. Each formulation was tested in two independent cells. The sorption voltage was chosen to ensure a driving force well above the onset of electrosorption across the whole series of electrodes and to make the differences in cycling behavior apparent within a practical number of cycles; it is not presented as an optimized operating point.

The salt adsorption capacity (*SAC*, mg·g^{-1}) was calculated using the formula (Equation (2)) [22]:

$$SAC = \frac{(C_0 - C_1)V}{m} \quad (2)$$

where C_0 is the initial concentration (1000 mg·L^{-1}), C_1 is the minimum concentration in the sorption cycle (mg·L^{-1}), V is the volume of circulating liquid (0.1 L), and m is the total mass of carbon material in both electrodes of the cell (0.85 of the mass of the carbon electrode for pristine materials and 0.8 for PANI-modified) (g). PANI was not included in the active mass, since the polymer is essentially non-porous (S_{BET} = 35.9 m^2 g^{-1}, Table 1) and contributes negligibly to the electrode surface area; SAC values normalized to the combined mass of carbon and PANI are given in Table S5 for comparison.

The electrical conductivity was converted into concentration values using pre-constructed calibration curves. For this purpose, solutions of the salts under investigation were prepared with concentrations of 6.25 × 10^{-3} mol·L^{-1}, 1.25 × 10^{-2} mol·L^{-1}, 2.5 × 10^{-2} mol·L^{-1}, 5 × 10^{-2} mol·L^{-1}, and 1 × 10^{-1} mol·L^{-1}, and the electrical conductivity was determined by pumping the calibration solution through the device. Carbon electrodes were not installed in the cell during the calibration process to eliminate any contribution from sorption. Data were processed and plotted using OriginPro 2021 (OriginLab Corporation, Northampton, MA, USA).

3. Results and Discussion

3.1. Carbon Material and PANI Characterization

The microstructure and morphology of AC-CW carbon was examined by SEM, revealing a typical structure of chemically activated carbons with heterogeneous grain sizes and a well-developed network of pores, including macropores up to 10 μm in diameter (Figure S2). The TC-MC carbon consists of relatively large (several hundred nm), compact fragments, yet the poor contrast indicates a porous texture without microporous net (Figure S2). The elemental mapping by SEM-EDX analysis of the pristine and modified electrodes are presented in Figure S3 and confirmed that both materials consisted predominantly of carbon and fluorine, the latter originating from the PTFE binder, with a combined content exceeding 97.5 at.%. Trace amounts of Fe and Cr were also detected in AC-CW and AC-CW-P samples, likely introduced during annealing in the iron reactor.

Sorption isotherms of pristine AC-CW and TC-MC carbons are summarized in Supplementary Materials and Table 1. The AC-CW isotherm (Figure S4) is of type I at low relative pressure, revealing the presence of micropores in the material, and of type IV at high relative pressure, typical for adsorbents having mesopores; the H2(a)-type hysteresis loop is related either to pore-blocking/percolation in a narrow range of pore necks or to cavitation-induced evaporation, and typically given by ordered mesoporous materials [23]. The isotherm of the TC-MC carbon (Figure S4) is a combination of type I at low relative pressure (presence of micropores) and type II at higher relative pressure, with a H3-type hysteresis loop [24], which characterizes the mesoporous aggregates formed by the MgO template; the lack of a plateau at high relative pressure, close to p/p_0 = 1, indicates the presence of macropores [23]. The specific surface area (SSA) values calculated on the basis of isotherms were 2941 m^2·g^{-1} and 1695 m^2·g^{-1} for AC-CW and TC-MC carbons, respectively. The micropore and mesopore volumes obtained from the NLDFT pore size distributions were 0.756 and 0.914 cm^3·g^{-1} for AC-CW and 0.307 and 1.794 cm^3·g^{-1} for TC-MC, respectively. The corresponding pore size distributions (Figure S4) quantify the difference between the two materials. In AC-CW the micropore mode is centered at 0.96 nm and micropores account for 45.3% of the total pore volume of 1.670 cm^3·g^{-1}, the remainder being distributed over narrow mesopores with a mode at 2.5 nm. In TC-MC the total pore volume is larger, 2.101 cm^3·g^{-1}; however, only 14.6% of it lies below 2 nm. The micropore mode is not resolved by nitrogen adsorption, with two resolved populations at 0.53 and 1.08 nm.

The polyaniline used for modification is essentially non-porous, with a BET surface area of 35.9 m^2 g^{-1} and a micropore volume of 0.007 cm^3 g^{-1}; its type II/III isotherm, with

most of the uptake above p/p_0 = 0.9, reflects condensation between non-porous fibers rather than intraparticle porosity. Comparison of the powders with the corresponding electrodes shows that electrode fabrication reduces the accessible surface area substantially: the BET area of AC-CW falls from 2941 to 2305 $m^2\ g^{-1}$ on forming, a reduction of 22% against the 15% expected from dilution by the binder alone, indicating that rolling with PTFE partially occludes the carbon surface. Incorporation of 5 wt% PANI, by contrast, changed the texture only marginally—the BET area of AC-CW decreased by a further 2.7% and its micropore volume by 2.4%, both smaller than the ~6% expected from simple dilution by the low-area polymer. The polymer therefore does not block the micropores; the pore architecture of the modified electrodes is that of the parent carbon, slightly diluted.

The Raman spectra of both carbons (Figure 1) exhibit the two characteristic bands of disordered graphitic materials: the D band, centered at 1349 cm^{-1} for AC-CW carbon and 1328 cm^{-1} for TC-MC carbon, and the G band at 1584 and 1582 cm^{-1}, respectively. The intensity ratios of these bands are nearly identical for the two materials (I_D/I_G = 1.44 and 1.42, respectively), taken as the ratio of the fitted D1 and G amplitudes. The difference between the two materials emerges instead from the band widths and from the deconvolution of the 800–2000 cm^{-1} region into its five conventional components (Figure 1 and Tables 2 and S1).

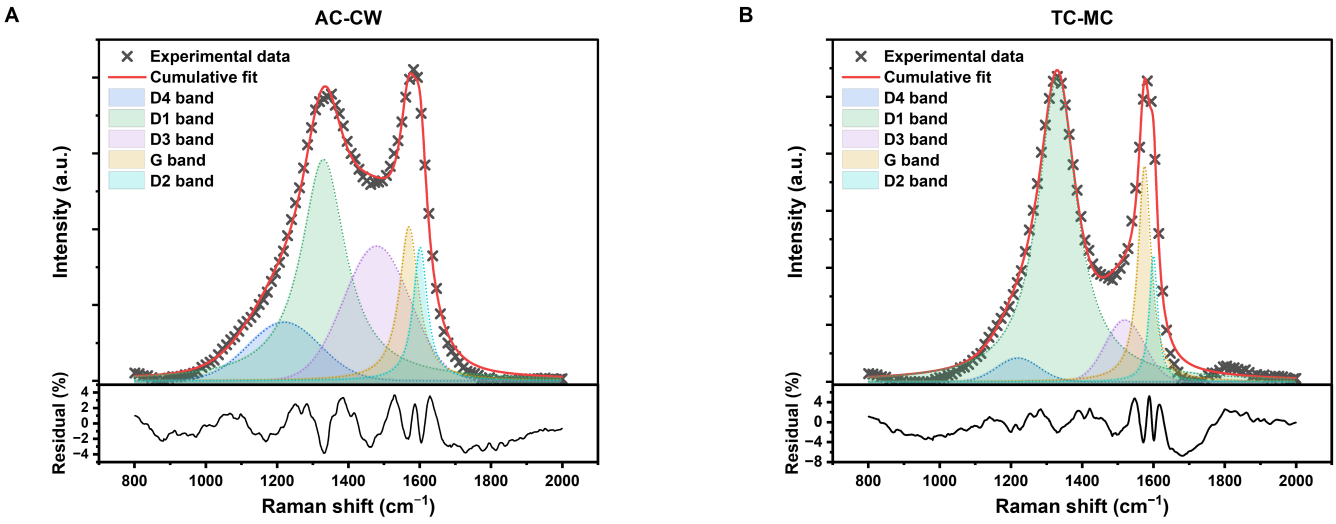


Figure 1. Deconvolution of the 800–2000 cm^{-1} region of AC-CW (**A**) and TC-MC (**B**) Raman spectra into the D4, D1, D3, G and D2 components.

Table 2. Derived structural parameters of carbons.

Material	D_{max}, cm^{-1}	G_{max}, cm^{-1}	I_D/I_G	A_{D1}/A_G	A_{D3+D4}	G, %
AC-CW carbon	1349	1584	1.44	3.35	37.3	12.6
TC-MC carbon	1328	1582	1.42	4.23	12.6	15.6

Note: I_D/I_G is the ratio of the fitted amplitudes of the D1 and G components.

The G band of TC-MC carbon is markedly narrower than that of AC-CW carbon (FWHM 44 vs. 64 cm^{-1}), as is its D1 band (131 vs. 150 cm^{-1}). In addition, the combined contribution of the D3 and D4 components—associated with amorphous sp^2 carbon and polyene- or sp^3-rich structures at the edges of graphitic domains, respectively—accounts for only 13% of the fitted area for TC-MC carbon, compared with 37% for AC-CW carbon. The degree of graphitization calculated using Equation (1) follows the same trend, reaching 15.6% for TC-MC carbon compared with 12.6% for AC-CW carbon. Consistent with its higher degree of structural order, only TC-MC exhibits detectable second-order Raman scattering, with a broad 2D band at 2663 cm^{-1} and a D + G combination band at 2901 cm^{-1},

whereas the AC-CW carbon spectrum is featureless above 1800 cm^{-1}. These structural differences can be attributed to the distinct synthesis routes. Carbonization of magnesium citrate generates the pore structure through template removal while leaving the carbon framework comparatively intact. In contrast, KOH activation forms the microporous network through chemical etching of the carbon lattice, which disrupts the graphitic domains and increases structural disorder, as reflected in the substantially larger D3 and D4 contributions observed for AC-CW carbon.

The FTIR and Raman spectra of the synthesized polymer (Figures S5 and S6, Tables S2 and S3) confirm the formation of polyaniline in the doped emeraldine salt form. In the IR, the pair of bands at 1552 and 1468 cm^{-1}, assigned to C=C stretching of the quinoid and benzenoid rings, is the characteristic signature of PANI, and their comparable intensities indicate a roughly equal proportion of oxidized and reduced units; C-N stretching of the secondary aromatic amine appears at 1285 cm^{-1}. The Raman spectrum is dominated by the in-plane C-H bending and the C-C stretching of the benzenoid ring at 1167 and 1593 cm^{-1}, with ring deformation modes at 414, 521 and 574 cm^{-1} and quinoid-ring deformations at 732 and 804 cm^{-1}. Both techniques show that the polymer is protonated and in its conducting state: the C-N^{+}• band of the polaron lattice appears at 1232 cm^{-1} in the infrared and at 1332 cm^{-1} in the Raman spectrum, the latter accompanied by the N-H bending mode of the protonated amine at 1507 cm^{-1}. The dominance of the out-of-plane C-H bending bands at 873 and 779 cm^{-1}, together with the absence of features characteristic of mono-substituted rings, indicates predominantly para-coupling of the aniline units and hence a linear chain structure, while the Raman band at 1375 cm^{-1} and the shoulder at 574 cm^{-1} point to a minor fraction of phenazine-like segments formed by partial cross-linking during polymerization. The presence of residual sulfate from the oxidant, detected by EDX only in the PANI-containing electrodes, is consistent with the polymer being obtained in a partially doped state.

3.2. Electrochemical Measurements

The voltammograms of the pristine carbons are close to rectangular over the whole range of scan rates (Figure 2A), with only a slight tilt developing at 50 mV s^{-1} and no discernible current peaks, which is common for charge storage dominated by EDL formation. Voltammograms and galvanostatic curves of the remaining materials are given in Figure S7. The PANI-containing electrodes behave differently: a broad pair of redox peaks appears in the range 0.15–0.35 V, superimposed on an otherwise rectangular envelope (Figure 2B). They correspond to the leucoemeraldine—emeraldine transition of polyaniline, which in acidic media is coupled to proton uptake and release. The peaks do not shift measurably with scan rate over 5–50 mV s^{-1}, indicating that this transformation is not kinetically hindered on the timescale of the measurement; since the measurements were performed in a symmetric two-electrode configuration, however, the peak positions correspond to cell voltages rather than to electrode potentials, and no further mechanistic assignment is attempted here. Their prominence and position in the stabilized voltammograms vary between nominally identical cells (Figure S8). Nevertheless, the capacitance enhancement associated with PANI is observed in every case. The presence of the redox peaks confirms that the polymer remains electroactive after incorporation into the composite electrode and that part of the charge stored by the modified electrodes is pseudocapacitive in origin.

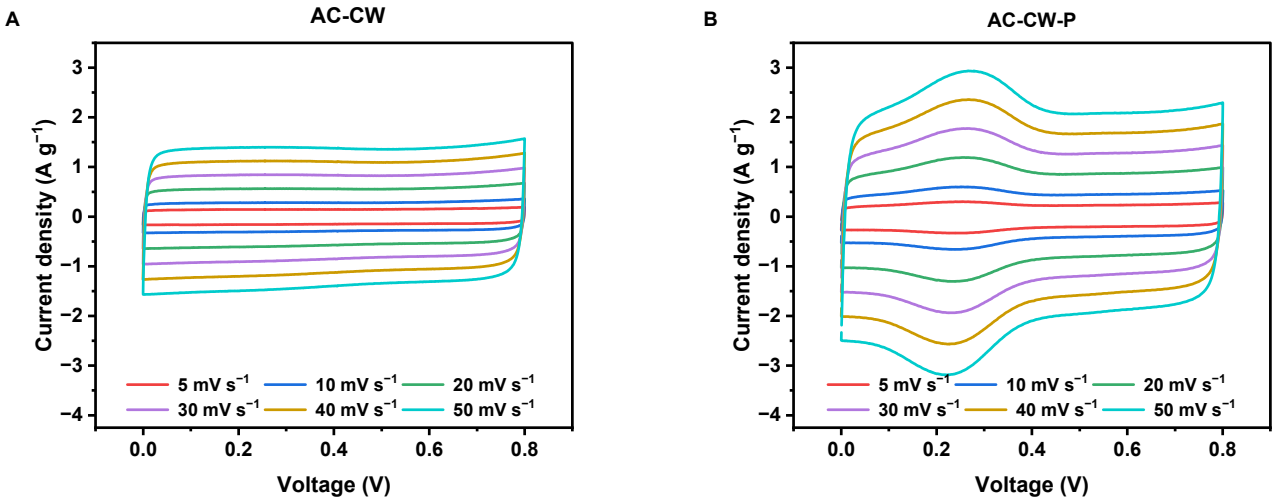


Figure 2. Cyclic voltammograms recorded at 5–50 mV s^{-1} in 1 M H_2SO_4 for (**A**) AC-CW and (**B**) AC-CW-P. The AC-CW-P show a pair of broad redox peaks superimposed on the rectangular envelope, corresponding to the RedOx transition of polyaniline.

The capacitances derived from the CVs and from the GCD curves are compared in Figure 3A and Table 3; values for the individual electrodes are given in Figure S9. The two techniques give the same ranking of the six materials over the whole range of scan rates and current densities. Among the pristine carbons, the microporous AC-CW delivered 224 F g^{-1} at 0.2 A g^{-1} and 249 F g^{-1} at 5 mV s^{-1}, against 159 and 165 F g^{-1} for the mesoporous TC-MC (Figure 3A). The 1.4–1.5-fold advantage of AC-CW follows from its higher specific surface area and dominant micropore volume (Table 1): narrow pores accommodate a much higher density of double-layer charge per unit mass, whereas wider mesopores contribute proportionally less surface for the same pore volume. The physical mixture of the two carbons behaved as a diluted version of its better component rather than as a synergistic composite. Its capacitance (202 F g^{-1} at 0.2 A g^{-1}, 216 F g^{-1} at 5 mV s^{-1}) lay between those of the parent materials, close to the value expected from a simple rule of mixtures, and did not exceed that of AC-CW at any scan rate or current density. The rate capability of the mixture was likewise no better than that of AC-CW alone (82% against 84% retention between 0.2 and 5 A g^{-1}), so the mesoporous fraction provided no kinetic benefit capable of compensating for the loss of microporous surface.

Table 3. Specific capacitance from CV and GCD (F g^{-1}).

Electrode	CV, 5 mV s^{-1}	CV, 50 mV s^{-1}	Retention, %	GCD, 0.2 A g^{-1}	GCD, 5.0 A g^{-1}	Retention, %
AC-CW	248.8 (+9.2/−15.9)	228.5 (+15.4/−7.9)	92	224.4 (+9.5/−7.5)	189.4 (+5.9/−6.7)	84
TC-MC	164.9 (+5.6/−8.4)	151.8 (+5.5/−9.4)	92	158.6 (+8.7/−7.6)	123.6 (+2.5/−4.7)	78
AC-CW + TC-MC	215.9 (+3.6/−3.2)	193.5 (+7.9/−6.8)	90	202.2 (+18.1/−10.8)	165.8 (+5.6/−3.7)	82
AC-CW-P	315.5 (+4.7/−4.9)	270.9 (+12.1/−10.1)	86	262.4 (+16.7/−25.1)	221.3 (+4.7/−4.7)	84
TC-MC-P	201.5 (+6.1/−10.4)	180.7 (+8.6/−7.6)	90	187.0 (+4.7/−4.7)	151.3 (+6.1/−6.1)	81
(AC-CW + TC-MC)-P	271.0 (+12.0/−17.6)	245.7 (+31.0/−24.6)	91	233.6 (+19.7/−20.6)	204.0 (+11.9/−6.4)	87

Note: Each value is the mean of three electrodes; the bracketed figures are the upper and lower bounds of the measured values rather than standard deviations.

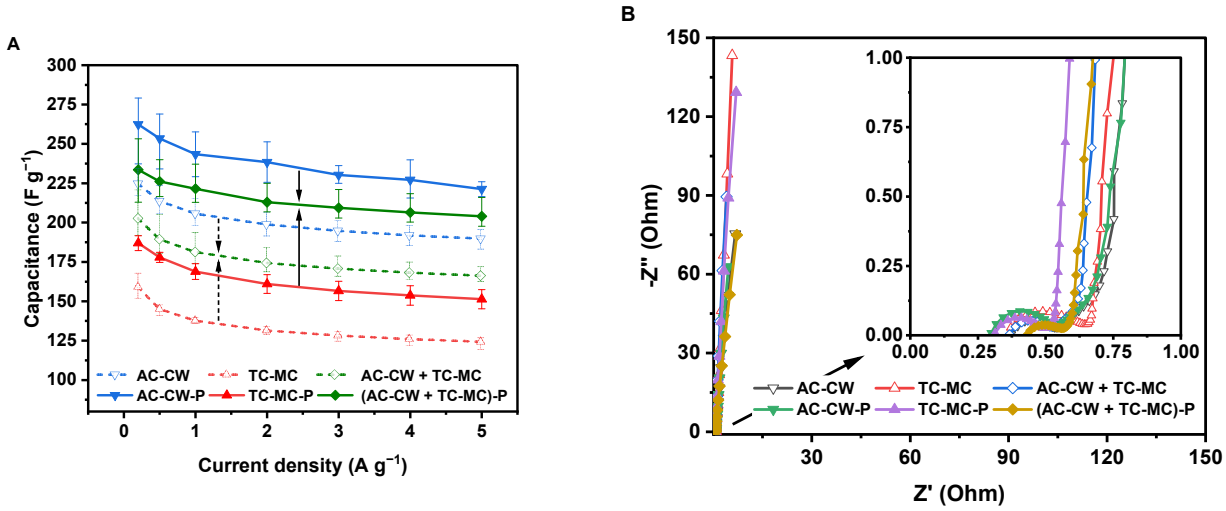


Figure 3. Electrochemical capacitances calculated from GCD measurements (**A**). Electrochemical impedance response of the pristine and PANI-modified electrodes: (**B**) Nyquist plots, inset showing the high-frequency region; the phase angle and the specific capacitance as functions of frequency are shown in Figure S10. For each material the curves are those of the electrode whose capacitance at 0.1 Hz was closest to the mean of the three replicates.

Addition of 5 wt% PANI raised the capacitance of all three carbons by a similar relative amount—17% for AC-CW, 18% for TC-MC and 16% for the mixture at 0.2 A g^{-1}—leaving the ordering of the materials unchanged, with AC-CW-P being the best electrode of the series at 262 F g^{-1} (0.2 A g^{-1}) and 316 F g^{-1} (5 mV s^{-1}). Attributing the whole increment to the polymer implies a specific capacitance of 454 to 608 F g^{-1} for the PANI fraction, which lies within the range reported experimentally for nanostructured polyaniline in sulfuric acid and well below its theoretical limit [25]. The enhancement is therefore consistent with a simple additive contribution of the pseudocapacitance of the polymer, with no evidence that the polymer alters the utilization of the carbon itself. Two independent observations support this reading: the series resistance is unchanged by the modification (Table 4), and the contact angles of the as-prepared electrodes (Table S4) show that the polymer does not render the surface more hydrophilic, increasing the contact angle in the case of the templated carbon. The rate capability of the modified electrodes was preserved (84–87% between 0.2 and 5.0 A g^{-1}, 86–91% between 5 and 50 mV s^{-1}), showing that the additional charge storage is not confined to slow processes.

Table 4. Parameters derived from electrochemical impedance spectroscopy of the pristine and PANI-modified carbon electrodes.

Electrode	R_s, Ohm	$\tau_0 = 1/f_{-45°}$, s	$C_{0.1Hz}$, F g^{-1}	φ_{min}, °
AC-CW	0.37 (+0.02/−0.03)	1.04 (+0.17/−0.14)	183 (+7/−14)	−84 (+3/−2)
TC-MC	0.37 (+0.05/−0.04)	0.49 (+0.05/−0.08)	131 (+17/−24)	−86 (+2/−1)
AC-CW + TC-MC	0.42 (+0.12/−0.06)	0.71 (+0.16/−0.11)	162 (+3/−2)	−86 (+1/−2)
AC-CW-P	0.53 (+0.44/−0.23) [a]	2.13 (+2.70/−1.57) [a]	203 (+21/−22)	−84 (+3/−2)
TC-MC-P	0.33 (+0.02/−0.02)	0.35 (+0.10/−0.12)	129 (+27/−36)	−85 (+4/−2)
(AC-CW + TC-MC)-P	0.37 (+0.06/−0.04)	0.98 (+0.38/−0.30)	211 (+29/−23)	−83 (+4/−2)

Notes: Each value is the mean of three electrodes; the bracketed figures are the upper and lower bounds of the measured values rather than standard deviations. R_s was taken as the real-axis intercept of the Nyquist plot, τ_0 as the reciprocal of the frequency at which the phase angle reaches −45°, and φ_{min} as the minimum phase angle reached in the low-frequency limit. [a] One of the three AC-CW-P cells showed a markedly higher series resistance (0.97 Ω), attributed to contact resistance, which also lengthened its response time (4.8 s); the other two cells gave R_s = 0.30 and 0.32 Ω and τ_0 = 1.00 and 0.57 s.

The impedance spectra (Figure 3B) are consistent with the picture above and resolve the kinetic difference between the two pore architectures that the quasi-static measurements do not. All six cells show the same overall shape: a small high-frequency feature followed by a steep, almost vertical low-frequency branch, with a minimum phase angle between −83° and −86° (Figure S10a), i.e., behavior close to that of an ideal capacitor. Above approximately 30 kHz the imaginary part of the impedance becomes negative and the phase angle positive; this is the inductive contribution of the cell and the connecting leads and does not reflect a property of the electrodes.

The equivalent series resistance, taken as the real-axis intercept, was 0.33–0.42 Ω for every material (Table 4); the higher mean value for AC-CW-P results from a single cell with elevated contact resistance, the other two cells giving 0.30 and 0.32 Ω (Table 4), i.e., independent of composition within the electrode-to-electrode scatter. PANI addition therefore does not measurably reduce the resistance of the electrode assembly, and the capacitance gain described above cannot be ascribed to improved electronic conduction.

The characteristic response time, defined as the reciprocal of the frequency at which the phase angle reaches −45°, orders the materials according to their pore architecture: 0.35 s for TC-MC-P and 0.49 s for TC-MC, 0.71 s for the mixture and 0.98 s for its PANI-modified counterpart, and 1.0 s for AC-CW and 0.6–1.0 s for AC-CW-P (excluding the high-resistance cell, Table 4). The micro-mesoporous carbon is thus intrinsically the faster material, as expected from its wider transport pores, and the mixture is intermediate, in proportion to its mesopore content. This kinetic advantage is realized only at frequencies at which the stored charge has already largely decayed, however, and it comes at the cost of a much lower low-frequency capacitance: at 0.1 Hz the values were 183 F g^{-1} for AC-CW against 131 F g^{-1} for TC-MC (Figure S10b). PANI modification left the response times essentially unchanged while raising the low-frequency capacitance of the coffee-waste carbon and of the mixture.

The capacitance increment produced by PANI in the impedance data at 0.1 Hz was not uniform: 11% for AC-CW, none within the scatter for TC-MC and 30% for the mixture, compared with 16–18% by GCD and 22–27% by CV (Tables 3 and 4). In a symmetric cell at 0 V both electrodes rest at the same but unknown potential, so the fraction of the redox capacity of the polymer accessed in the impedance measurement cannot be specified, and these differences are not interpreted further. The pseudocapacitive origin of the additional charge is indicated by the redox peaks in the voltammograms (Figures 2B and S8); its magnitude, however, depends on the technique and on the carbon, i.e., unlike the double-layer capacitance of the carbons, the contribution of the polymer is not a single well-defined quantity.

The long-term stability of the electrodes was assessed by galvanostatic cycling at 2 A g^{-1} over 10,000 cycles (Figure S11). All six formulations proved essentially stable, retaining between 95 and 100% of their initial capacitance, with coulombic efficiencies that rose over the first few hundred cycles and then remained constant at 98.9–99.6% for the remainder of the test. The differences between the materials are marginal and do not follow the composition: the PANI-containing electrodes retained 95.3, 96.7 and 98.8% against 96.4, 99.6 and 99.7% for their pristine counterparts, so within the electrochemical stability window the polymer confers no measurable stability benefit. The gradual increase in retention observed over the first several hundred cycles for most of the electrodes parallels the development of the redox features during the initial conditioning and is likewise attributed to the progressive access of the electrolyte to the electrode volume.

Measurements in the CDI feed. The response of the electrodes in 1 g L^{-1} NaCl over 0–1.6 V is summarized in Figure 4 and Table 5; individual curves are in Figures S12–S14 and Table S7. The series resistance rose to 43–126 Ω, more than two orders of magnitude above that in acid, and the voltammograms lost their rectangular shape above about 5 mV s^{-1} (Figure S12).

At comparable rates (5 mV s^{-1}, 0.2 A g^{-1}) the capacitance of the pristine electrodes was 34–52% of that in acid (Table 3 and Table S7), with the same ranking by every technique: AC-CW > AC-CW + TC-MC > TC-MC (119, 93 and 62 F g^{-1} at 2 mV s^{-1}). The mesoporous carbon showed no rate advantage either: between 2 and 50 mV s^{-1} the pristine electrodes retained 26–31% of their capacitance, and between 0.2 and 1 A g^{-1} AC-CW retained 79% against 60% for TC-MC (Figure S14). With one cell per formulation, differences within the cell-to-cell scatter in acid (about ±10%, Table 3) are not considered significant.

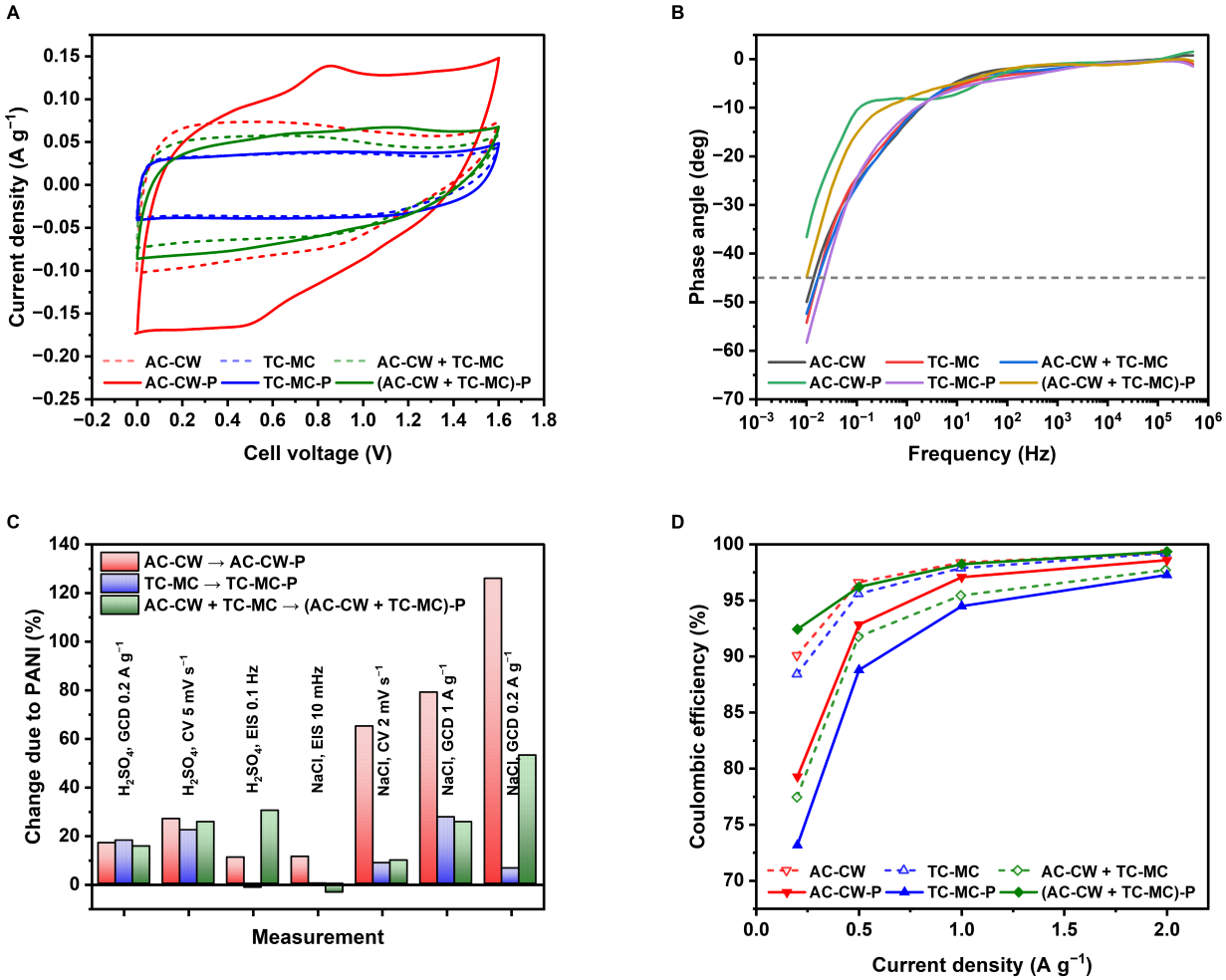


Figure 4. Electrochemical behavior of the six electrodes in 1 g L^{-1} NaCl over the 0–1.6 V window: (**A**) cyclic voltammograms at 2 mV s^{-1}; (**B**) phase angle as a function of frequency at 0 V, the symbols marking the frequency at which the phase angle reaches −45°; (**C**) change in capacitance produced by 5 wt% PANI for each carbon, measured in H_2SO_4 and in NaCl by different techniques; (**D**) coulombic efficiency of GCD as a function of current density. One cell per formulation.

Impedance at 0 V (Figure 4B, Table 5) shows much slower ion transport than in acid: the phase angle reached −45° only at 14–23 mHz, i.e., τ_0 = 44 s for TC-MC-P, 59 s for TC-MC and the mixture, and 72 s for AC-CW, 70–130 times longer than in 1 M H_2SO_4 (Table 4). For AC-CW-P and (AC-CW + TC-MC)-P the phase angle stayed above −45° down to 10 mHz (−37° and −45°, respectively), so that $\tau_0 \geq 100$ s; AC-CW-P also had the highest loading (4.6 mg cm^{-2}), which lengthens the transport path. The differences between the carbons are small compared with the effect of the electrolyte. The relation of these response times to the 10 min CDI half-cycle is discussed in Section 3.3; for the two PANI electrodes with $\tau_0 \geq 100$ s the margin relative to the half-cycle is smaller.

Table 5. Electrochemical parameters of the electrodes in 1 g L^{-1} NaCl (cell voltage 0–1.6 V; EIS at 0 V).

Electrode	C_{CV}, F g^{-1} (2 mV s^{-1})	C_{GCD}, F g^{-1} (0.2 A g^{-1})	CE_{GCD}, % (0.2 A g^{-1})	$C_{10\ mHz}$, F g^{-1}	R_s, Ω	τ_0, s	$\varphi_{10\ mHz}$, °
AC-CW	119	116	90	121	43	72	−50
TC-MC	62	53	88	61	81	59	−54
AC-CW + TC-MC	93	72	77	82	64	59	−52
AC-CW-P	197	262	79	134	67	≥100	−37
TC-MC-P	68	57	73	61	87	44	−58
(AC-CW + TC-MC)-P	102	111	92	80	126	≥100	−45

Notes: One cell per formulation, measured in the sequence CV, GCD, EIS. Capacitances are per electrode and normalized to the active mass; CE_{GCD} is the coulombic efficiency of GCD; $C_{10\ mHz}$ was calculated from the imaginary part of the impedance at 10 mHz; τ_0 is the reciprocal of the frequency at which the phase angle reaches −45°; for AC-CW-P and (AC-CW + TC-MC)-P the phase angle did not reach −45° above 10 mHz. Values at other rates are given in Table S7.

PANI remained only partly electroactive in the neutral electrolyte. AC-CW-P shows a broad anodic wave at about 0.86 V (2 mV s^{-1}) without a resolved cathodic counterpart (Figure 4A); unlike the peaks in acid, it shifted strongly with scan rate (to 1.19 V at 20 mV s^{-1}), and the spectrum contains a depressed arc of about 40 Ω at 1–10 Hz that is absent from the pristine electrodes (Figure S13). No such features were resolved for TC-MC-P and (AC-CW + TC-MC)-P. The capacitance change due to PANI therefore depended strongly on the carbon and the technique (Figure 4C): +11% at 10 mHz, +65% by CV at 2 mV s^{-1} and +126% by GCD at 0.2 A g^{-1} for AC-CW-P, i.e., growing with the time spent at high voltage; 0 and +9% (10 mHz, 2 mV s^{-1}) and +6 to +28% by GCD for TC-MC-P; and −4 and +10% and +25 to +53% by GCD for the mixture. Part of the extra charge was not recovered on discharge: at 0.2 A g^{-1} the coulombic efficiency fell from 90 to 79% for AC-CW and from 88 to 73% for TC-MC, but rose from 77 to 92% for the mixture (Figure 4D). In the feed, the contribution of the polymer is therefore neither the uniform 16–18% measured in acid nor fully reversible. How these results relate to salt adsorption is discussed in Section 3.4.

3.3. CDI Measurements of Pristine Carbons

The cycling results for the pristine electrodes in 1 g L^{-1} NaCl solution are presented in Figure 5. Throughout the paper, the conductivity profiles (Figures 5A–C and 6A–C) are shown for the first cell of each formulation; those of the second cell are given in Figure S16, and the SAC of both cells in Figure S15. In all cases, a typical saw-tooth CDI response was observed throughout the 100 cycles, confirming stable cell operation. The mean baseline conductivity remained constant within ±1% over the entire experiment for all electrodes, indicating complete desorption at 0 V and the absence of irreversible salt accumulation. However, the amplitude of the oscillations decreased continuously with cycling.

Among the pristine carbons, the microporous AC-CW exhibited the highest salt adsorption capacity, with a SAC_{MAX} of 34.7 mg g^{-1}, whereas the mesoporous TC-MC reached 17.4 mg g^{-1}. This trend is consistent with the electrochemical measurements, in which AC-CW also exhibited the highest specific capacitance, and with its larger specific surface area and dominant micropore volume (Table 1). The origin of this difference is largely geometric: for slit-shaped pores the surface area available per unit pore volume scales as 2/w, so that a given volume distributed in 1 nm pores offers several times the area it would offer in 4 nm pores. The two carbons illustrate this directly: although the TC-MC electrode has the larger total pore volume (1.95 against 1.35 cm^3 g^{-1}), its DFT surface area per unit pore volume is less than half that of AC-CW (585 against 1272 m^2 cm^{-3}, Table 1). In the narrowest pores this is reinforced by the overlap of the double layers of the opposing walls, which suppresses co-ion expulsion and thereby raises the charge efficiency, whereas

the interior of a wider pore remains essentially electroneutral bulk solution and stores no net charge. The 1:1 physical mixture of the two carbons showed no synergistic effect under the present conditions. Its SAC_{MAX} of 23.9 mg g^{-1} was intermediate between those of the individual components and slightly below the value predicted by a simple rule of mixtures. Thus, the mesoporous component primarily acted as a diluent of the microporous carbon rather than as a transport-enhancing additive [1]. Impedance measurements in the feed solution are consistent with this interpretation (Section 3.2): although ion transport in 1 g L^{-1} NaCl is about two orders of magnitude slower than in acid, the response times of the three pristine electrodes (59–72 s) are 8–10 times shorter than the 10 min half-cycle and differ little between the carbons, and the mesoporous carbon showed no rate advantage in NaCl. Under the present operating conditions—low flow rate and a 10 min half-cycle—ion transport into the electrode is therefore unlikely to be the main limitation, so the additional diffusion pathways offered by the mesopores bring no measurable benefit, whereas the associated loss of micropore volume directly lowers the storage capacity. Since the time constant of the CDI cell itself was not measured, this conclusion refers to the electrode materials rather than to the cell as a whole. Other mixing ratios, and operation at higher flow rates or shorter half-cycles, where ion transport may become limiting, were not examined and could behave differently.

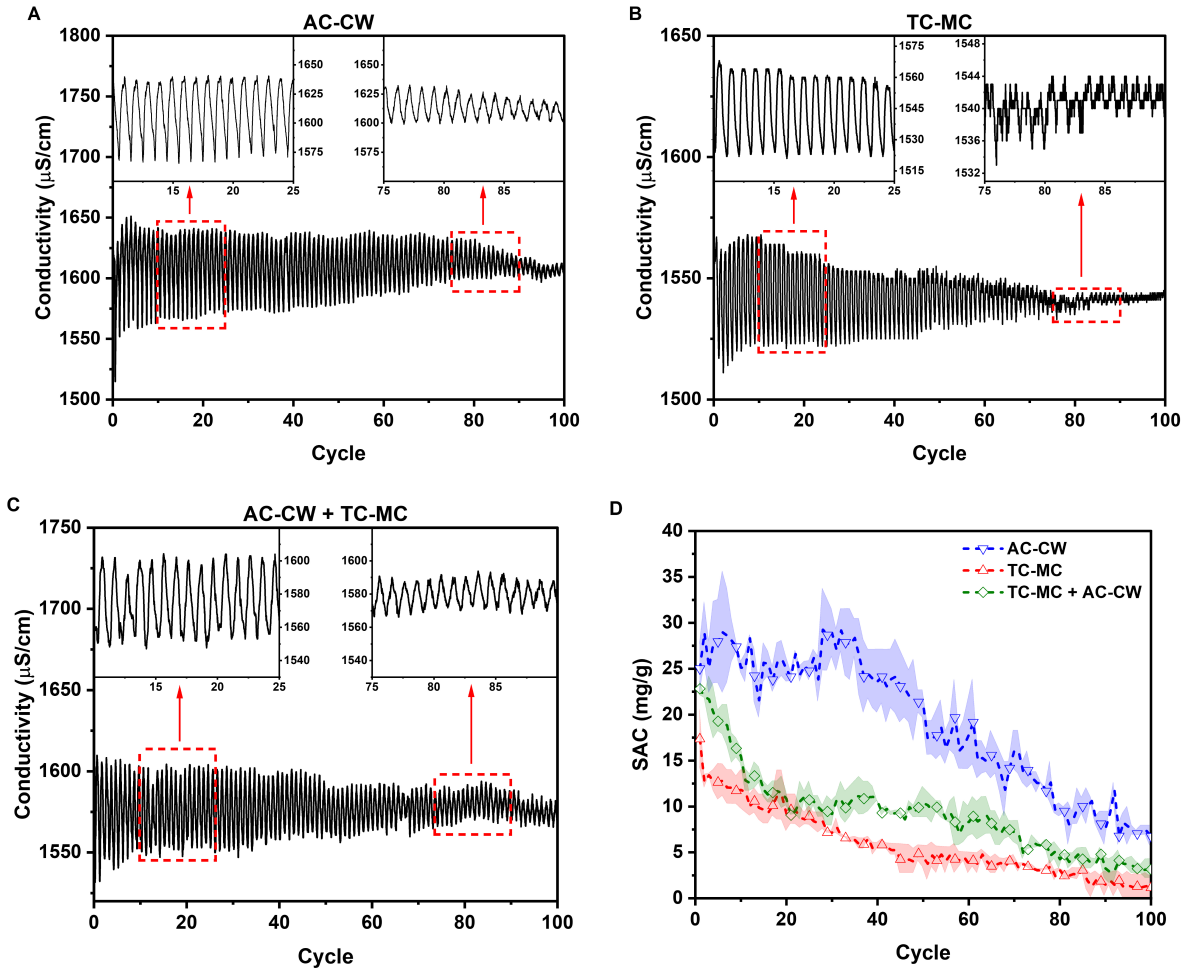


Figure 5. Cycling stability of pristine AC-CW (**A**), TC-MC (**B**) and AC-CW + TC-MC (**C**) electrodes and SAC evolution (**D**) during CDI operation. Conductivity profiles (**A**–**C**) are shown for the first cell; SAC in (**D**) is the mean of two independent cells (individual cells in Figures S15 and S16).

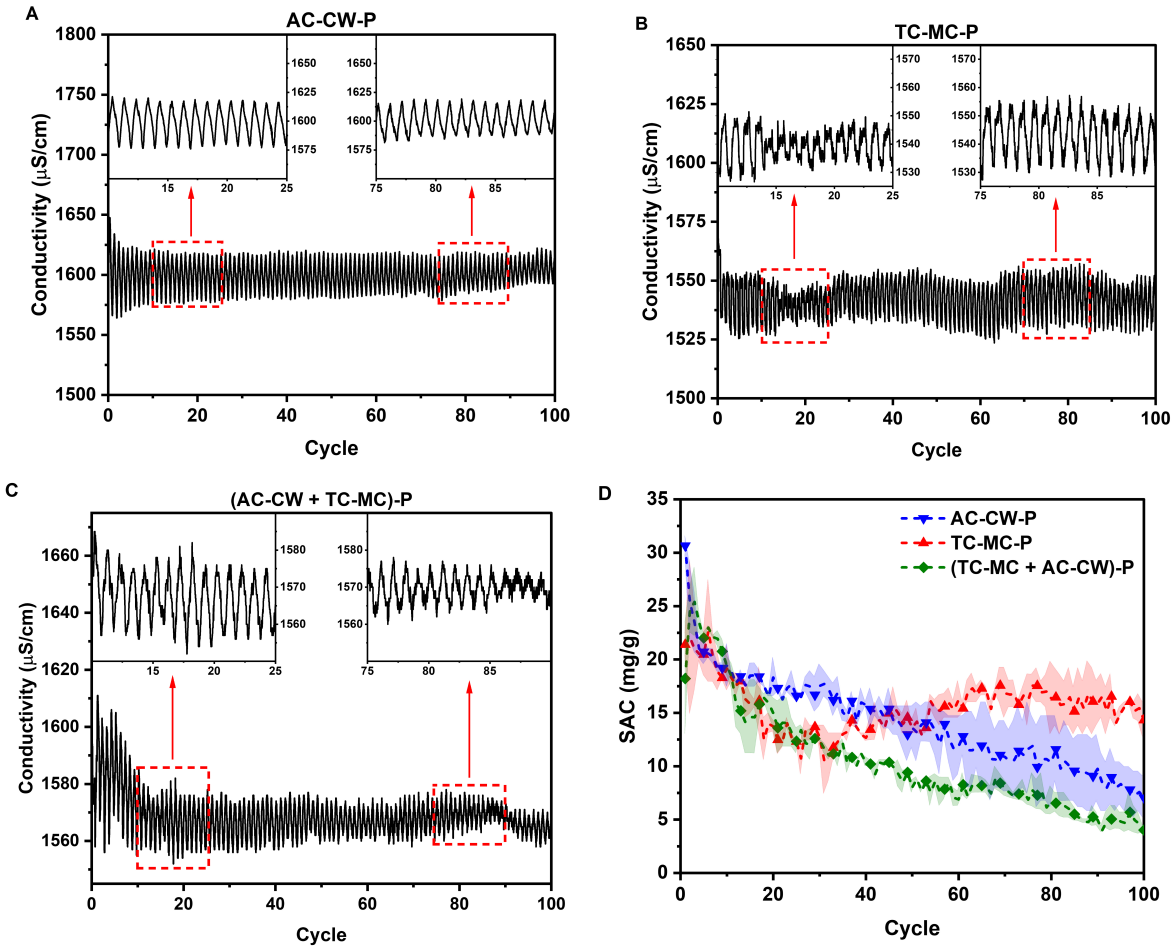


Figure 6. Cycling stability of PANI-modified AC-CW-P (**A**), TC-MC-P (**B**) and (AC-CW + TC-MC)-P (**C**) electrodes and SAC evolution (**D**) during CDI operation. Conductivity profiles (**A**–**C**) are shown for the first cell; SAC in (**D**) is the mean of two independent cells (individual cells in Figures S15 and S16).

All three pristine cells exhibited severe performance degradation. The SAC decreased to below half of its initial value by cycles 55–77 for AC-CW, 32–48 for TC-MC, and 21–23 for the AC-CW + TC-MC mixture (two cells each). After 100 cycles, the corresponding mean SAC retentions were only 29%, 12%, and 18%, respectively. Because the degradation primarily affects the amplitude of the CDI response while the baseline conductivity remains unchanged, it is more consistent with a progressive loss of electrochemically accessible surface area than with changes in the feed composition. Operation at +1.6 V, which exceeds the thermodynamic stability window of water, is known to promote Faradaic side reactions at the positive electrode, including carbon oxidation accompanied by oxygen evolution [26,27]. In carbon CDI electrodes, such processes have been reported to generate oxygen-containing surface functionalities that reduce the effective capacitance, increase electrode resistance and promote co-ion expulsion [12]. Whether this mechanism operates in the present electrodes is examined in Section 3.4. If it does, the near-complete deactivation of TC-MC may be related to its lower total surface area, which would make a comparable absolute extent of oxidative damage proportionally more detrimental to its electrochemically accessible surface and, consequently, to its adsorption capacity.

3.4. CDI Measurements of Modified Carbons

Figure 6 presents the cycling behavior of the PANI-modified electrodes in 1 g L^{-1} NaCl solution. In contrast to the pristine AC-CW and TC-MC samples, the conductivity oscillations

of TC-MC-P remained almost undamped. The effect of 5 wt% polyaniline on the initial capacity did not follow the uniform capacitance gain measured in acid: the maximum SAC decreased from 34.7 to 30.7 mg·g^{-1} for AC-CW-P but increased from 17.4 to 24.8 mg g^{-1} for TC-MC-P, the latter with a large scatter between the two cells (20.4 and 29.3 mg g^{-1}). This is not because the polymer is inactive in the neutral feed: the capacitance gain at the CDI voltage was largest for AC-CW-P, whose SAC decreased (by 12% for SAC_{MAX} and 19% for the mean over cycles 1–10), and smallest for TC-MC-P, whose SAC increased (by 43% and 59%, respectively; Section 3.2, Figure 4C). The additional electrochemical charge therefore does not translate into salt storage, and for the two single carbons the two quantities even change in opposite directions. Two contributions can account for this. First, part of the additional charge is irreversible (Figure 4D) and is consumed by faradaic processes—oxidation of the polymer, the carbon or the electrolyte—that remove no salt [28]. Second, in a neutral chloride solution the charge of the polymer can be compensated either by uptake of Cl^-, which contributes to desalination, or by release of protons, which does not [29]; since the pH was not monitored during cycling, the two pathways cannot be distinguished here. The origin of the higher initial SAC of TC-MC-P therefore remains unclear and, given the scatter between cells, should be treated with caution.

The benefit of the modification lies in the cycling stability, and it is unambiguous only for the templated carbon. After a break-in period of 10–20 cycles the SAC of TC-MC-P stabilized at about 15 mg·g^{-1} and remained essentially unchanged up to cycle 100. PANI modification raised the mean retained capacity from 12% to 76% for the templated carbon. For the coffee-waste carbon the mean retention rose only from 29% to 36%, within the scatter between the two AC-CW-P cells (27% and 45%), and both electrodes reached the same residual SAC of about 8 mg g^{-1} over cycles 91–100. Two contributions may explain this stabilizing role, although neither could be verified directly with the present data: the conducting polymer may act as a redox buffer that partially shields the carbon surface from irreversible anodic oxidation at +1.6 V, and its fibrous morphology may maintain an electronically percolating network as the carbon surface chemistry evolves, limiting the loss of electrochemically addressable area that dominates the fading of the pristine electrodes. Since the polymer confers no stability benefit within the electrochemical window (Section 3.2), its stabilizing effect in the CDI cell is specific to the conditions of the desalination experiment; protection of the carbon surface against anodic over-oxidation at +1.6 V is a plausible, though unconfirmed, origin, rather than any intrinsic reinforcement of the electrode [9,30]. The measurements in NaCl show that this stabilization is not associated with a smaller irreversible charge: TC-MC-P had the lowest coulombic efficiency of the series at 0.2 A g^{-1} (73%) yet the highest SAC retention, whereas (AC-CW + TC-MC)-P, with the highest efficiency (92%), retained only 22%.

PANI did not improve the performance of the mixed-carbon electrode (Table 6). The (AC-CW + TC-MC)-P electrode reached a maximum SAC of 26.0 mg·g^{-1}, with an average SAC of 22.1 mg·g^{-1} over the first 10 cycles, but retained only 22% of this value after 100 cycles, against 18% for the unmodified AC-CW + TC-MC mixture, i.e., no improvement within the scatter between cells. This confirms that, in the 1:1 physical blend studied here, the two carbons do not act cooperatively and that the polymer cannot compensate for the loss of micropore volume.

The morphology of the electrodes was examined by SEM before and after 100 cycles (Figure S17). In every case the images were indistinguishable within the typical variation between regions of the same electrode: the angular, plate-like carbon particles retained smooth faces and sharp edges; no cracking, delamination or formation of a distinct surface product was observed. For the pristine electrodes, which lost most of their capacity over the test, this excludes physical disintegration as the origin of the fading and points to changes

that are not resolved by SEM, such as a change in surface chemistry. For the PANI-modified electrodes the same observation shows no sign that the polymer is lost from the electrode during prolonged operation at +1.6 V, which argues against a mechanical origin of its stabilizing role.

Table 6. Desalination performance of the pristine and PANI-modified carbon electrodes over 100 charge/discharge cycles.

Electrode	SAC_{MAX}, mg g^{-1}	$SAC_{av.\ 1–10}$, mg g^{-1}	$SAC_{av.\ 91–100}$, mg g^{-1}	Retention *,%	Cumulative SAC over 100 Cycles, mg g^{-1}
AC-CW	34.7 ± 0.9	27.3 ± 2.7	8.0 ± 0.4	29 ± 1	1897 ± 77
TC-MC	17.4 ± 3.1	12.9 ± 1.4	1.4 ± 1.2	12 ± 10	578 ± 7
AC-CW + TC-MC	23.9 ± 0.3	19.2 ± 1.3	3.4 ± 0.8	18 ± 6	915 ± 61
AC-CW-P	30.7 ± 0.9	22.0 ± 0.8	7.9 ± 2.2	36 ± 9	1407 ± 153
TC-MC-P	24.8 ± 4.5	20.5 ± 2.6	15.4 ± 0.3	76 ± 8	1558 ± 84
(AC-CW + TC-MC)-P	26.0 ± 2.6	22.1 ± 0.0	4.8 ± 0.9	22 ± 4	1047 ± 21

Notes: * Retention = $SAC_{av.\ 91–100}/SAC_{av.\ 1–10} \times 100\%$. Cumulative SAC is the sum of the per-cycle values over cycles 1–100. Each value is the mean of two independent cells ± half the difference between them; retention was calculated for each cell and then averaged.

The wettability of the electrodes was assessed by water contact angle measurements before and after 100 CDI cycles (Figure 7, Table S4). All as-prepared electrodes were hydrophobic, with contact angles between 121 and 133°, consistent with the presence of the PTFE binder, and the droplet profile was stable over the whole measurement, indicating a non-absorbing surface. After cycling, the three pristine formulations became markedly more hydrophilic: the mean contact angle (four electrodes from two independent cells, Table S4) fell by 37° for AC-CW, 26° for the mixture and 22° for TC-MC, whereas the two PANI-modified single-component electrodes were essentially unchanged (−4° for TC-MC-P and +6° for AC-CW-P). The values were reproducible between the two cells of each formulation to within 3°.

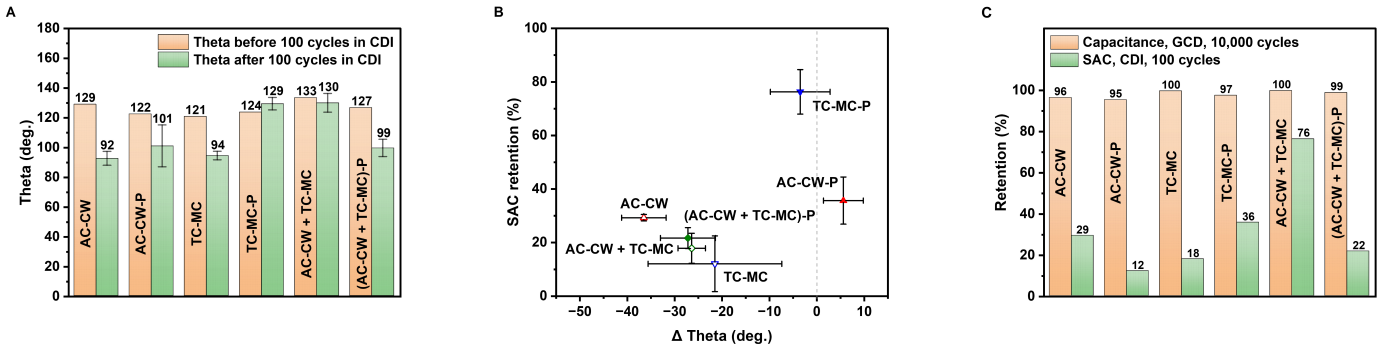


Figure 7. Water contact angles of the electrodes before and after 100 CDI cycles: (**A**) mean values of four electrodes (two electrodes from each of two independent cells), with the individual values shown as horizontal marks; (**B**) change in contact angle plotted against the SAC retention after 100 cycles. Capacity retention of the six electrode formulations after 100 CDI cycles at +1.6 V and after 10,000 GCD cycles at 2 A g^{-1} within a 0.8 V window (**C**).

For AC-CW and the mixture, both electrodes of each cell were affected to a similar extent; for TC-MC, one electrode of each cell changed much more than the other (by about 34° against 9°), consistently in both cells. One possible explanation is that the desorption step was carried out at an enforced cell voltage of 0 V rather than at open circuit: short-circuiting equalizes the potentials of the two electrodes but need not return either of them to its original value, since irreversible charge accumulated during sorption can shift the common potential, so that over many cycles the negative electrode may also be exposed to

oxidizing potentials. The change in wettability cannot at present be assigned to a specific surface reaction (see the FTIR results below).

The magnitude of this change is associated with the desalination stability across the series (Figure 7B): the four formulations whose mean contact angle decreased by more than 20° retained 29% or less of their initial SAC, whereas the two whose contact angle changed by less than 10° retained 36 and 76%. The PANI-modified mixed-carbon electrode follows the same pattern, its contact angle falling by 27° and its retention reaching only 22%, consistent with the absence of any stabilizing effect of the polymer in the mixed-carbon system. With only six formulations, and with the retentions of AC-CW and AC-CW-P differing within the scatter between cells, this is a qualitative association rather than a quantitative correlation, and it does not by itself establish a causal link. An increase in hydrophilicity would be the expected consequence of the accumulation of oxygen-containing surface functionalities [29,31]. Whether such groups formed in the present electrodes is examined by FTIR below. It should also be noted that the cycled electrodes were exposed to a large volume of water and dried at 105 °C before measurement, and that no unpolarized control was measured; the contributions of the electrochemical treatment and of the handling procedure cannot therefore be fully separated. The absence of any comparable change in the two single-carbon PANI-modified electrodes, which underwent an identical procedure, nevertheless argues against handling alone as the origin of the effect.

The surface chemistry of the cycled electrodes was examined by FTIR, separately for the positive and negative electrode of each cell (Figure S18, Table S6). No systematic increase in the carbonyl band at about 1730 cm^{-1} or in the C-O stretching region was found after cycling for any of the electrodes, and the remaining differences in band intensity were within the variation between spectra caused by sample contact. FTIR therefore provides no direct evidence for the accumulation of oxygen-containing groups invoked above, although changes confined to the outermost surface may lie below its detection limit. The characteristic bands of PANI (1552, 1468 and 1285 cm^{-1}, Table S2) were not resolved against the carbon background at 5 wt% loading, either before or after cycling, so the state of the polymer cannot be assessed from these spectra. The only distinct change was the appearance, on the negative electrodes of TC-MC and TC-MC-P, of a broad band at about 1430 cm^{-1} accompanied by sharp bands at 877 and 712 cm^{-1}, a combination characteristic of the ν_3, ν_2 and ν_4 vibrations of the carbonate ion in calcite [32]. The three bands grew together, 5–10-fold relative to the as-prepared electrodes, and were absent from the positive electrodes of the same cells; for (AC-CW + TC-MC)-P the signal was at the limit of detection, and no carbonate was detected on the other electrodes. Since the templated carbon contains no magnesium after acid washing (EDX, Figure S3), the deposit most likely originates from Ca^{2+} present as an impurity in the feed and precipitates at the negative electrode, where the reduction in dissolved oxygen and water raises the local pH during charging [28]. Its preferential formation on TC-MC may be related to the large meso- and macropore volume of this carbon, which offers space for nucleation, whereas nucleation in the ~1 nm micropores of AC-CW is restricted.

The contrast with the electrochemical cycling experiments (Figure 7C) should be interpreted with caution, because the two tests differ in several respects at once: the electrolyte (1 M H_2SO_4 against 1 g L^{-1} NaCl) and hence the pH and ionic strength; the maximum cell voltage (0.8 against 1.6 V); the mode of operation (galvanostatic cycling at 2 A g^{-1} without dwell against potentiostatic holding at +1.6 V for 10 min, so that the electrodes spend far longer at the maximum voltage); the cell (a sealed Swagelok cell against a flow-through cell fed from an open reservoir, i.e., with dissolved oxygen and traces of Ca^{2+}); and the number of cycles and total duration. Under the first set of conditions the materials retained more than 95% of their capacitance after 10,000 cycles, whereas under

the second the pristine electrodes lost most of their capacity within 100 cycles. The fading observed in the desalination experiments is therefore not an intrinsic instability of the electrode materials but a consequence of the operating conditions. Of these, the cell voltage beyond the stability window of water is the most likely dominant factor: GCD in the NaCl feed up to 1.6 V gave coulombic efficiencies of only 73–92% at 0.2 A g^{-1}, against 98.9–99.6% in acid within 0.8 V, and the voltammograms showed a rising anodic current above about 1.4 V (Figure S12), so irreversible faradaic processes do take place at the CDI voltage in this electrolyte. The absence of any morphological change after cycling (Figure S17) indicates that the fading is not caused by physical degradation of the electrode; the underlying change in surface chemistry, however, could not be identified by FTIR.

Taken together, the results reveal a clear trade-off between initial adsorption capacity and long-term cycling stability, as illustrated by the Pareto plots (Figure 8). Pristine AC-CW represents one extreme of the Pareto front, combining the highest initial capacity in the series (27.3 mg g^{-1} over the first 10 cycles) with a relatively low retention of only 29% after 100 cycles. At the opposite extreme, TC-MC-P retains 76% of its initial capacity, but starts from a lower SAC of 20.5 mg g^{-1}. AC-CW-P occupies an intermediate position in Figure 8B, retaining 36% of its initial 22.0 mg g^{-1}, and thus represents a compromise between the two criteria; its residual SAC after 100 cycles, however, does not differ from that of pristine AC-CW (7.9 and 8.0 mg g^{-1}, Figure 8A). The remaining electrodes, including both mixed-carbon systems, are simultaneously inferior in both objectives, indicating that, for the 1:1 blend and the conditions studied here, physical blending offers no advantage over the better-performing component regardless of the relative weighting assigned to initial capacity and stability. The practical implications are illustrated by the cumulative SAC over 100 cycles, represented by the marker size in Figure 8. Pristine AC-CW delivers the highest total salt removal (1897 mg g^{-1}), but its output declines rapidly with cycling. In contrast, AC-CW-P achieves a cumulative removal of 1407 mg g^{-1} and TC-MC-P of 1558 mg g^{-1}, 2.7 times that of pristine TC-MC (578 mg g^{-1}); of the two, only TC-MC-P maintains a stable performance. TC-MC-P surpasses all pristine samples after approximately 60 cycles and removes more salt than any other electrode over cycles 51–100 (799 against 622 mg g^{-1} for AC-CW), making cycling stability the decisive factor for sustained continuous operation.

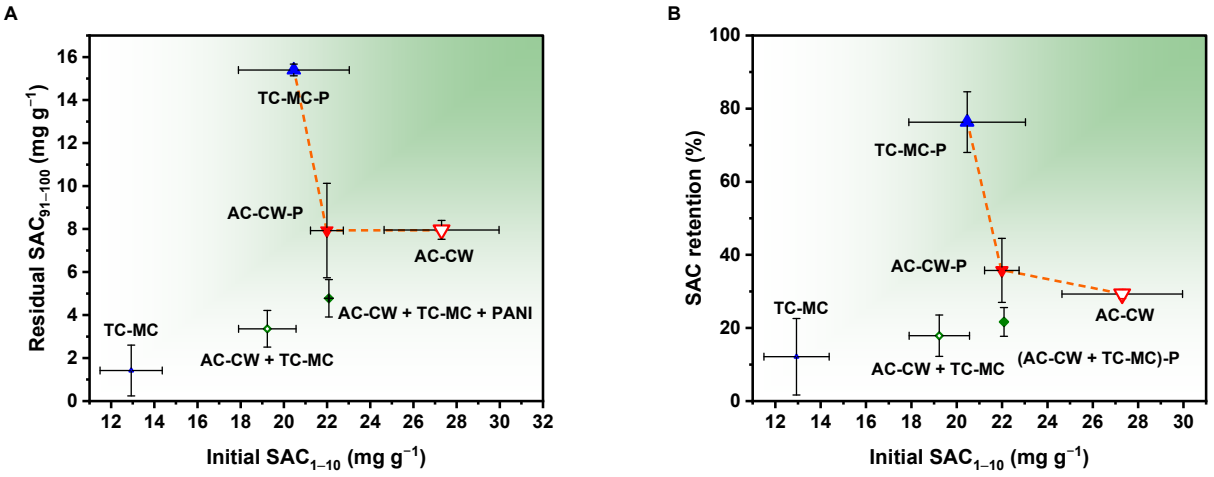


Figure 8. Capacity-stability trade-off in the studied CDI electrodes: mean SAC over cycles 1–10 vs (**A**) residual SAC averaged over cycles 91–100 and (**B**) capacity retention after 100 cycles. Marker size is proportional to the cumulative salt removed over 100 cycles.

Whether the electrochemical measurements could have anticipated these results is examined in Figure 9. For the three pristine electrodes, the capacitance ranked the initial SAC correctly irrespective of the electrolyte and the technique (AC-CW > AC-CW + TC-MC

> TC-MC), so that for the purely capacitive carbons of the present series a capacitance measurement provided a valid first screening. The PANI-modified electrodes did not follow this correspondence in either electrolyte: in acid the polymer raised the capacitance of the three carbons by a similar amount, whereas the mean SAC over cycles 1–10 changed by −19, +59 and +15%, and in NaCl the capacitance gain was largest where the SAC decreased. Of the measurements compared, the reversible capacitance in the feed at 0 V (EIS at 10 mHz) came closest to the SAC ranking, whereas slow charging up to 1.6 V in NaCl overstated the contribution of AC-CW-P, part of whose charge was irreversible. None of the electrochemical measurements, in either electrolyte, anticipated the durability observed in CDI: all formulations retained 95–100% of their capacitance after 10 000 cycles in acid, and neither the capacitance nor the coulombic efficiency in NaCl (Table 5) ranked the SAC retention (Table 6).

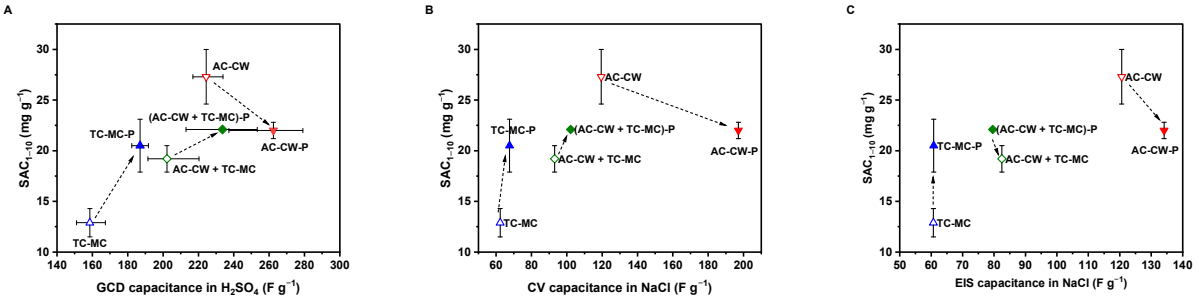


Figure 9. SAC vs GCD capacitance in H_2SO_4 (**A**), CV capacitance in NaCl (**B**) and EIS capacitance in NaCl (**C**).

Two limitations of the present data should be noted. First, the current and the pH of the solution were not recorded during the CDI experiments, so neither the charge efficiency nor the energy consumption can be calculated, and salt adsorption cannot be separated quantitatively from faradaic reactions—a distinction of particular relevance for the PANI-containing electrodes. The coulombic efficiencies measured in NaCl provide only an indirect indication: at 0.2 A g^{-1}, 8–27% of the charge passed up to 1.6 V was not recovered on discharge, the lowest efficiencies being found for TC-MC-P (73%), AC-CW + TC-MC (77%) and AC-CW-P (79%), so a part of the current in the CDI cell must be expected to be faradaic as well. Second, the stabilization by PANI was assessed at a single cell voltage, and a practical assessment would require tests at lower cell voltages, at which the pristine electrodes degrade more slowly and the advantage of the polymer may be smaller, together with measurements of current, pH and energy consumption per unit of salt removed; this trade-off between driving voltage, energy consumption and long-term salt removal lies beyond the scope of the present comparison.

4. Conclusions

The two carbons behaved as their textures predicted: the microporous coffee-waste carbon delivered 224 F g^{-1} against 159 F g^{-1} for the micro-mesoporous templated carbon (GCD in 1 M H_2SO_4), and this ordering was reproduced by all three electrochemical techniques, in acid and in the NaCl feed, and carried over to the initial salt adsorption capacity. Their 1:1 physical mixture showed no synergy under the present conditions, falling close to the rule of mixtures. Because ion transport is unlikely to limit the ten-minute CDI half-cycle, the mesoporous fraction brought no measurable benefit, while the micropore volume it displaced was lost.

Incorporation of 5 wt% polyaniline raised the capacitance of all three carbons by 16–18% in sulfuric acid (GCD), consistent with an additive contribution of the polymer. In the NaCl feed at the CDI voltage its contribution depended on the carbon and on the

technique, was partly irreversible (coulombic efficiencies of 73–79% at 0.2 A g^{-1} for TC-MC-P and AC-CW-P), and was largest for the coffee-waste carbon, whose salt adsorption capacity decreased, and smallest for the templated carbon, whose salt adsorption capacity increased. What the polymer changed was the retention of the capacity, which rose from 12% to 76% for the templated carbon over 100 cycles (means of two cells), whereas for the coffee-waste carbon the change (29% to 36%) was within the scatter between cells.

None of the electrochemical measurements anticipated this behavior. Cycled galvanostatically 10 000 times within a 0.8 V window; all six formulations retained 95–100% of their capacitance. At +1.6 V in the CDI cell the pristine electrodes lost most of their capacity within 100 cycles, with unchanged morphology but contact angles falling by 37, 26 and 22° for AC-CW, the mixture and TC-MC, respectively, while the two single-carbon PANI electrodes showed no comparable change. The loss is associated with the operating conditions rather than with an intrinsic instability of the materials; the cell voltage is the most likely, though not the only, cause, since the electrolyte, pH and mode of operation also differed between the two tests.

Capacitance is therefore a useful but limited descriptor of a CDI electrode. For the purely capacitive carbons of the present series it ranked the initial salt adsorption capacity correctly, regardless of the electrolyte and the technique, and can serve for a first screening of such materials. It failed once a pseudocapacitive component was introduced, in acid and in the feed alike, and it predicted the durability of none of the electrodes. The six electrodes lie on a capacity-stability trade-off, with pristine AC-CW at one extreme, TC-MC-P at the other and AC-CW-P between them, and the choice between them follows from the intended duty cycle rather than from the capacitance.

These conclusions rest on two parent carbons, their mixture and one polymer additive at a single loading, with one electrochemical cell per formulation in NaCl, and are not proposed as a general rule. Whether capacitance ranks the initial salt adsorption capacity of purely capacitive carbons in general, and how other pseudocapacitive or faradaic components affect this correspondence, needs to be tested on a broader set of electrodes differing systematically in pore structure, surface chemistry and composition, preferably with the current, pH and charge efficiency recorded during CDI operation.

Supplementary Materials: The following supporting information can be downloaded at: https://www.mdpi.com/article/10.3390/w18212729/s1, Figure S1: CDI cell scheme; Figure S2: SEM images of pristine AC-CW carbon (S2.1), TC-MC carbon (S2.2) and PANI (S2.3); Figure S3: EDX spectra of the AC-CW (S3.1), TC-MC (S3.2), AC-CW-P (S3.3) and TC-MC-P (S3.4) electrodes before cycling; Figure S4: Nitrogen adsorption–desorption isotherms at 77 K and pore size distributions of the pristine AC-CW and TC-MC carbons; Figure S5: ATR-FTIR spectrum of the PANI nanofibers synthesized by bicontinuous microemulsion polymerization; Figure S6: Raman spectrum of the PANI nanofibers recorded with 785 nm excitation; Figure S7: Typical cyclic voltammograms recorded at 5–50 mV s^{-1} and GCD curves recorded at 0.5–5 A g^{-1} for the six electrodes in 1 M H_2SO_4; Figure S8: Cyclic voltammograms of the individual PANI-containing electrodes recorded at 5–50 mV s^{-1}; Figure S9: Specific capacitance of the individual electrodes as a function of current density (GCD) and scan rate (CV); Figure S10: Phase angle and specific capacitance as functions of frequency for the pristine and PANI-modified electrodes in 1 M H_2SO_4; Figure S11: Capacitance retention and coulombic efficiency of the six electrode formulations over 10,000 GCD cycles at 2 A g^{-1}; Figure S12: Cyclic voltammograms and GCD curves recorded in 1 g L^{-1} NaCl over the 0–1.6 V window; Figure S13: Impedance spectra of the six electrodes in 1 g L^{-1} NaCl at 0 V; Figure S14: Specific capacitance of the six electrodes in 1 g L^{-1} NaCl as a function of scan rate (CV) and current density (GCD); Figure S15: SAC values of both CDI cells with pristine and PANI-modified electrodes; Figure S16: Conductivity profiles of the second set of cells (cell 2) during 100 CDI cycles at +1.6 V; Figure S17: SEM images of the six electrodes before and after the long-cycling CDI test (S17.1–S17.12); Figure S18: FTIR spectra of

the electrodes before cycling and of the positive and negative electrodes after 100 CDI cycles at +1.6 V; Table S1: Raman parameters of the carbon materials; Table S2: Assignment of the ATR-FTIR bands of the synthesized PANI nanofibers; Table S3: Assignment of the Raman bands of the synthesized PANI nanofibers (785 nm excitation); Table S4: Water contact angles of the electrodes before and after 100 CDI cycles (two independent cells per formulation); Table S5: Desalination performance of the electrodes with SAC normalized to the combined mass of carbon and PANI; Table S6: Assignment of the FTIR bands of the electrodes before and after 100 CDI cycles; Table S7: Electrochemical parameters of the electrodes in 1 g L^{-1} NaCl.

Author Contributions: A.Y.Z.—Conceptualization, Investigation, Data curation, Writing—original draft, Writing—editing; S.D.—Investigation, Data curation; G.V.A.—Investigation, Data curation; G.Z.—Data curation; Z.A.—Data curation, Writing—editing; S.A.—Data curation; V.V.P.—Conceptualization, Supervision, Writing—review; N.N.—Conceptualization, Supervision. All authors have read and agreed to the published version of the manuscript.

Funding: This research was funded from the Science Committee of the Ministry of Science and Higher Education of the Republic of Kazakhstan (Scientific Research Grants no. AP22786994 and BR28713323).

Data Availability Statement: The data that support the findings of this study are available on request from the corresponding author. The data are not publicly available due to privacy or ethical restrictions.

Conflicts of Interest: Authors Georgiy V. Alexan and Vladimir V. Pavlenko were employed by the company Carbonix Group LLP. The remaining authors declare that the research was conducted in the absence of any commercial or financial relationships that could be construed as a potential conflict of interest.

References

1. Porada, S.; Borchardt, L.; Oschatz, M.; Bryjak, M.; Atchison, J.S.; Keesman, K.J.; Kaskel, S.; Biesheuvel, P.M.; Presser, V. Direct Prediction of the Desalination Performance of Porous Carbon Electrodes for Capacitive Deionization. *Energy Environ. Sci.* **2013**, *6*, 3700–3712. [CrossRef]
2. Baroud, T.N.; Giannelis, E.P. Role of Mesopore Structure of Hierarchical Porous Carbons on the Electrosorption Performance of Capacitive Deionization Electrodes. *ACS Sustain. Chem. Eng.* **2019**, *7*, 7580–7596. [CrossRef]
3. Liu, G.-W.; Fan, C.-S.; Hsu, C.-H.; Hou, C.-H.; Lin, H.-P. Optimizing the Micro/Mesoporous Structure of Hierarchical Porous Carbon Synthesized from Petroleum Pitch Using the Solvent-Free Method for Ultra-Fast Capacitive Deionization. *ACS Omega* **2022**, *7*, 47610–47618. [CrossRef] [PubMed]
4. Lin, Y.; Ma, J.; Liu, W.; Li, Z.; He, K. Efficient Removal of Dyes from Dyeing Wastewater by Powder Activated Charcoal/Titanate Nanotube Nanocomposites: Adsorption and Photoregeneration. *Environ. Sci. Pollut. Res.* **2019**, *26*, 10263–10273. [CrossRef] [PubMed]
5. Lu, D.; Cai, W.; Wang, Y. Optimization of the Voltage Window for Long-Term Capacitive Deionization Stability. *Desalination* **2017**, *424*, 53–61. [CrossRef]
6. Geng, C.; Gao, Y.; Ming, H.; Duan, D.; Meng, J.; Gao, W.; Shen, X.; Liu, S.; Lv, J.; Xi, J.; et al. Continuous Cycling of Carbon-Based Capacitive Deionization Systems: An Evaluation of the Electrode Performance and Stability. *J. Electroanal. Chem.* **2022**, *914*, 116298. [CrossRef]
7. Wang, C.; Ren, L.-F.; Ying, D.; Jia, J.; Shao, J. Enhancing Performance of Capacitive Deionization under High Voltage by Suppressing Anode Oxidation Using a Novel Membrane Coating Electrode. *J. Membr. Sci.* **2022**, *652*, 120506. [CrossRef]
8. Hawks, S.A.; Ramachandran, A.; Porada, S.; Campbell, P.G.; Suss, M.E.; Biesheuvel, P.M.; Santiago, J.G.; Stadermann, M. Performance Metrics for the Objective Assessment of Capacitive Deionization Systems. *Water Res.* **2019**, *152*, 126–137. [CrossRef] [PubMed]
9. Gao, X.; Omosebi, A.; Landon, J.; Liu, K. Surface Charge Enhanced Carbon Electrodes for Stable and Efficient Capacitive Deionization Using Inverted Adsorption–Desorption Behavior. *Energy Environ. Sci.* **2015**, *8*, 897–909. [CrossRef]
10. Algurainy, Y.; Call, D.F. Improving Long-Term Anode Stability in Capacitive Deionization Using Asymmetric Electrode Mass Ratios. *ACS EST Eng.* **2021**, *2*, 129–139. [CrossRef]
11. Pavlenko, V.V.; Zakharov, A.Y.; Ayaganov, Z.E.; Mansurov, Z.A. Nanoporous Carbon Materials: Modern Production Methods and Applications. *Russ. Chem. Rev.* **2024**, *93*, RCR5122. [CrossRef]

12. Evans, S.F.; Ivancevic, M.R.; Wilson, D.J.; Hood, Z.D.; Adhikari, S.P.; Naskar, A.K.; Tsouris, C.; Paranthaman, M.P. Carbon Polyaniline Capacitive Deionization Electrodes with Stable Cycle Life. *Desalination* **2019**, *464*, 25–32. [CrossRef]
13. Wang, H.; Liu, Y.; Li, Y.; Xu, X.; Liu, X.; Yao, Y.; Lu, T.; Pan, L. Tactics for Boosting the Desalination Stability of Capacitive Deionization. *Chem. Eng. J.* **2024**, *496*, 153808. [CrossRef]
14. Supiyeva, Z.; Avchukir, K.; Pavlenko, V.; Yeleuov, M.; Taurbekov, A.; Smagulova, G.; Mansurov, Z. The Investigation of Electroreduction of AuCl4-AuCl4- in the Case of Gold Electrosorption Using Activated Carbon. *Mater. Today Proc.* **2020**, *25*, 33–38. [CrossRef]
15. Morishita, T.; Tsumura, T.; Toyoda, M.; Przepiórski, J.; Morawski, A.W.; Konno, H.; Inagaki, M. A Review of the Control of Pore Structure in MgO-Templated Nanoporous Carbons. *Carbon* **2010**, *48*, 2690–2707. [CrossRef]
16. Askar, P.; Kanzhigitova, D.; Ospanova, A.; Tapkharov, A.; Duisenbekov, S.; Abutalip, M.; Soltabayev, B.; Turlybekuly, A.; Adilov, S.; Nuraje, N. 1 Ppm-Detectable Hydrogen Gas Sensor Based on Nanostructured Polyaniline. *Sci. Rep.* **2024**, *14*, 26984. [CrossRef] [PubMed]
17. Zakharov, A.Y.; Tukesheva, A.V.; Ayaganov, Z.Y.; Aidarkhanov, D.; Ng, A.; Pavlenko, V.V. Development of Photovoltaic-Powered Autonomous MCDI System for Heavy Metals Removal. *Results Eng.* **2026**, *30*, 111138. [CrossRef]
18. Chen, W.-C.; Wen, T.-C.; Teng, H. Polyaniline-Deposited Porous Carbon Electrode for Supercapacitor. *Electrochim. Acta* **2003**, *48*, 641–649. [CrossRef]
19. Stakhanova, S.V.; Krechetov, I.S.; Shafigullina, K.E.; Lepkova, T.L.; Berestov, V.V.; Statnik, E.S.; Zyryanova, Z.E.; Novikova, E.A.; Korsunsky, A.M. Hierarchically Porous Carbon Cloth–Polyaniline (CC–PANI) Composite Supercapacitor Electrodes with Enhanced Stability. *Crystals* **2024**, *14*, 457. [CrossRef]
20. Jagiello, J.; Olivier, J.P. 2D-NLDFT Adsorption Models for Carbon Slit-Shaped Pores with Surface Energetical Heterogeneity and Geometrical Corrugation. *Carbon* **2013**, *55*, 70–80. [CrossRef]
21. Sadezky, A.; Muckenhuber, H.; Grothe, H.; Niessner, R.; Pöschl, U. Raman Microspectroscopy of Soot and Related Carbonaceous Materials: Spectral Analysis and Structural Information. *Carbon* **2005**, *43*, 1731–1742. [CrossRef]
22. Silva, A.P.; Argondizo, A.; Juchen, P.T.; Ruotolo, L.A.M. Ultrafast Capacitive Deionization Using Rice Husk Activated Carbon Electrodes. *Sep. Purif. Technol.* **2021**, *271*, 118872. [CrossRef]
23. Thommes, M.; Kaneko, K.; Neimark, A.V.; Olivier, J.P.; Rodriguez-Reinoso, F.; Rouquerol, J.; Sing, K.S.W. Physisorption of Gases, with Special Reference to the Evaluation of Surface Area and Pore Size Distribution (IUPAC Technical Report). *Pure Appl. Chem.* **2015**, *87*, 1051–1069. [CrossRef]
24. Sing, K.S.W.; Williams, R.T. Physisorption Hysteresis Loops and the Characterization of Nanoporous Materials. *Adsorpt. Sci. Technol.* **2004**, *22*, 773–782. [CrossRef]
25. Li, H.; Wang, J.; Chu, Q.; Wang, Z.; Zhang, F.; Wang, S. Theoretical and Experimental Specific Capacitance of Polyaniline in Sulfuric Acid. *J. Power Sources* **2009**, *190*, 578–586. [CrossRef]
26. Cohen, I.; Avraham, E.; Bouhadana, Y.; Soffer, A.; Aurbach, D. Long Term Stability of Capacitive De-Ionization Processes for Water Desalination: The Challenge of Positive Electrodes Corrosion. *Electrochim. Acta* **2013**, *106*, 91–100. [CrossRef]
27. Uwayid, R.; Seraphim, N.M.; Guyes, E.N.; Eisenberg, D.; Suss, M.E. Characterizing and Mitigating the Degradation of Oxidized Cathodes during Capacitive Deionization Cycling. *Carbon* **2021**, *173*, 1105–1114. [CrossRef]
28. Kang, J.S.; Kim, S.; Kang, J.; Joo, H.; Jang, J.; Jo, K.; Park, S.; Kim, H.; Yoo, S.J.; Yoon, J.; et al. Surface Electrochemistry of Carbon Electrodes and Faradaic Reactions in Capacitive Deionization. *Environ. Sci. Technol.* **2022**, *56*, 12602–12612. [CrossRef] [PubMed]
29. Arulrajan, A.C.; Dykstra, J.E.; Van Der Wal, A.; Porada, S. Unravelling pH Changes in Electrochemical Desalination with Capacitive Deionization. *Environ. Sci. Technol.* **2021**, *55*, 14165–14172. [CrossRef] [PubMed]
30. Bahdanchyk, M.; Hashempour, M.; Sarı, Z.T.; Vicenzo, A. Electrochemical Study of Charging Processes and Cycling Degradation of Bare and Ion-Exchange Membrane-Coated Microporous Activated Carbon Electrodes for Capacitive Deionization. *Electrochim. Acta* **2025**, *519*, 145829. [CrossRef]
31. Balaji-Wright, A.; Wu, J.; Shocron, A.N.; Dana, A.G.; Suss, M.; Mani, A. Understanding Degradation of Capacitive Deionization Cells: Full–Cell Simulations with Anode Corrosion. *Desalination* **2024**, *587*, 117924. [CrossRef]
32. Andersen, F.A.; Kralj, D. Determination of the Composition of Calcite-Vaterite Mixtures by Infrared Spectrophotometry. *Appl. Spectrosc.* **1991**, *45*, 1748–1751. [CrossRef]

Disclaimer/Publisher's Note: The statements, opinions and data contained in all publications are solely those of the individual author(s) and contributor(s) and not of MDPI and/or the editor(s). MDPI and/or the editor(s) disclaim responsibility for any injury to people or property resulting from any ideas, methods, instructions or products referred to in the content.